SURFACE PLASMON MICROSCOPY OF INHOMOGENEOUS AQUEOUS MIXTURES

MICROSCOPIE DE PLASMONS DE SURFACE DES MÉLANGES AQUEUX INHOMOGÈNES

A Thesis Submitted to the Division of Graduate Studies of the Royal Military College of Canada by

Yevgeniy Mikhyeyev
Capt

In Partial Fulfillment of the Requirements for the Degree of Master of Science in Physics

April 2019

Acknowledgments

I would like to thank my supervisor Dr. Ribal Georges Sabat, for his infinite patience and trust and for guiding me through all stages of the research. I would also like to thank my group members and my family for their advice and encouragement.

Abstract

In the last decade, the field of photonics has seen a great deal of research in the use of nanostructures to excite surface plasmon resonance (SPR) on metal-dielectric interfaces. Nowadays, various applications benefit from this phenomenon where an incident light beam causes an electromagnetic resonance characterized by electron density fluctuations at a metal-dielectric interface. One of these applications is SPR microscopy. The most widely used excitation technique for SPR microscopy is the prism coupling method. This work presents a different approach, which uses crossed surface relief gratings (CSRG) for SPR microscopy. The CSRG fabrication is based on direct laser interference patterning applied on azobenzene molecular glass thin films using a Lloyd's mirror interferometer. Two superimposed perpendicular constant-pitch linear gratings are fabricated and then they are coated with a 60-nm layer of silver. The resulting metallic CSRG has the ability to transmit light in a very narrow bandwidth when placed in between two orthogonal linear polarizers due to a unique SPR light polarization conversion phenomenon. In this work, this SPR effect is used for obtaining polarization-contrast microscopy images of water-based inhomogeneous mixtures placed on the CSRG's surface. A series of imaging experiments were carried out using a variety of water-based inhomogeneous mixtures when the samples were illuminated by coherent and incoherent light at a wavelength of 632.8 nm. The static and video microscopy images resulting from these experiments were analyzed in terms of their brightness and contrast with respect to the CSRG parameters, as well as their ability to image and detect various analytes or inhomogeneities in water. Also, first-ever direct imaging of the SPR wave propagation along a metal-dielectric interface was performed. The obtained SPR propagation length was found to be in agreement with the theoretical results. Two-dimensional demonstration of the plasmonic energy exchange and the polarization conversion in a CSRG was carried out.

Résumé

Au cours de la dernière décennie, de nombreuses recherches ont été faites dans le domaine de la photonique sur l'utilisation de nanostructures pour exciter la résonance de plasmon de surface (RPS) sur des interfaces métal-diélectrique. De nos jours, diverses applications tirent profit de ce phénomène lorsqu'un faisceau lumineux incident provoque une résonance électromagnétique caractérisée par des fluctuations de la densité des électrons à une interface métal-diélectrique. Une de ces applications est la microscopie RPS. La technique d'excitation RPS la plus largement utilisée pour la microscopie RPS est la méthode de couplage par prisme. Ce travail présente une approche différente qui utilise des réseaux de diffraction croisés (RDC) pour la microscopie RPS. La fabrication du RDC est basée sur la structuration de films minces d'azobenzène de verre moléculaire par interférence directe d'un laser à l'aide d'un interféromètre à miroir de Lloyd. Deux réseaux linéaires perpendiculaires à pas constant superposés sont fabriqués puis recouverts d'une couche d'argent de 60 nm. Le RDC métallique résultant a la capacité de transmettre la lumière dans une bande passante très étroite lorsqu'il est placé entre deux polariseurs linéaires orthogonaux en raison d'un phénomène unique de conversion de polarisation de la lumière RPS. Dans ce travail, cet effet RPS est utilisé pour obtenir des images de microscopie à contraste de polarisation de mélanges inhomogènes à base d'eau placés à la surface du RDC. Une série d'expériences d'imagerie a été réalisée en utilisant une variété de mélanges inhomogènes à base d'eau lorsque les échantillons ont été éclairés par une lumière cohérente et incohérente à une longueur d'onde de 632,8 nm. Les images statiques et les vidéos de microscopie résultantes de ces expériences ont été analysées en termes de luminosité et de contraste par rapport aux paramètres RDC, ainsi que de leur capacité à visualiser et à détecter divers analytes ou inhomogénéités dans l'eau. En outre, la toute première imagerie directe de la propagation de l'onde RPS le long d'une interface métal-diélectrique a été réalisée. La longueur de propagation du RPS obtenue était en accord avec les résultats théoriques. Une démonstration bidimensionnelle de l'échange d'énergie plasmonique et de la conversion de polarisation dans un CSRG a été effectuée.

Contents

List of Tables

List of Figures

List of Abbreviations

AFM	Atomic Force Microscope
CSRG	Crossed Surface Relief Grating
gDR1	Disperse Red 1 Molecular Glass
RI	Refractive Index
PDMS	Polydimethylsiloxane
SPP	Surface Plasmon Polariton
SPR	Surface Plasmon Resonance
SPRi	Surface Plasmon Resonance imaging
SPRM	Surface Plasmon Resonance Microscopy
SRG	Surface Relief Grating
TE	Transverse Electric (linearly polarized light)
TM	Transverse Magnetic (linearly polarized light)

List of Symbols

Greek Symbols

Symbol	Description	Definition
δ	Skin depth	
ε	Dielectric permittivity of a material	
ε_0	Dielectric permittivity of free space	$\sim 8.854 \times 10^{-12} F \cdot m^{-1}$
ε_r	Relative dielectric permittivity of a material	$\varepsilon/\varepsilon_0$
θ	Angular resolution	
θ_i	Angle of incidence	
θ_m	Angle of diffraction order	
λ	Wavelength of light	
λ_{sp}	Surface plasmon wavelength	
μ	Magnetic permeability of a material	
μ_0	Magnetic permeability of free space	$\sim 1.257 \times 10^{-6}\ N/A^2$
μ_r	Relative magnetic permeability of a material	μ/μ_0
ρ	Volume charge density	

Symbol	Description	Definition
τ	Mean time between electron collisions in a metal	
ω	Angular frequency	
ω_p	Bulk plasma frequency of a metal	
ω_{max}	Characteristic plasmon frequency	
Δ	Optical path difference between two light	
	beams	
Λ	Grating pitch	

Roman Symbols

Symbol	Description	Definition
c	The speed of light in vacuum	$\sim 3.0 \times 10^8\, m/s$
D	Optical device aperture	
d_{min}	Diffraction limit	
e	The elementary charge	$1.602176634 \times 10^{-19}\, C$
$\boldsymbol{E}$	Electric field vector	
$\boldsymbol{H}$	Magnetic field vector	
$\boldsymbol{J}$	Current density	
k	Wave number	$2\pi/\lambda$
$\boldsymbol{k}$	Wave vector	
k_0	Light wave number in free space	
k_{sp}	Surface plasmon wave number	
$\boldsymbol{K}$	Grating vector	
m	Diffraction order	
m_e	The electron mass	$\sim 9.109 \times 10^{-31} kg$
n	Refractive index of a material	
n_e	Conduction electrons density	
q	Grating depth	
t	Time	
v	Wave velocity	$v = \omega/k$

Additional Notations

Notation	Description
A	Scalar
$\boldsymbol{A}$	Vector
A_x	x-component of the vector A
A_y	y-component of the vector A
$A_{\boldsymbol{z}}$	z-component of the vector A
$\tilde{A}$	Complex number
A'	Real part of $\tilde{A}$
A''	Imaginary part of $\tilde{A}$
A_d	Quantity in a dielectric
A_m	Quantity in a metal

1 Introduction

The study of optical phenomena emerging during metals' surface interaction with electromagnetic radiation is called plasmonics or nanoplasmonics. This rapidly growing field of science is associated with the control of electromagnetic waves on a sub-wavelength scale. Over the past few years, many innovative concepts and applications based on this phenomenon have been developed.

1.1 Brief History of Surface Plasmons Discovery

In 1902, American physicist and inventor Robert Williams Wood observed a significant intensity drop for certain wavelengths of light reflected from a metal diffraction grating under the condition of light polarization parallel to the grating vector [1]. Even though he noticed that these anomalies took place only when the sample had been irradiated by polarized light, it was Fano who some years later understood that they were caused by surface waves ("Fano waves") [2].

The notion of Surface Plasmon Polariton (SPP) was introduced only a half-century after Wood's discovery. The SPP phenomenon has been known from the works of A. Sommerfeld [3, 4]. In 1953, D. Pines and D. Bohm [5] introduced the term "surface plasmons". Later, the name of Surface Plasmon Resonance (SPR) became more commonly used, although the SPP still appears in multiple sources.

A theoretical substantiation of the existence of SPRs at an interface between a metal and a dielectric was given by R. Ritchie in 1957 [6]. Several years later, E. Stern and R. Ferrell obtained a dispersion relation connecting frequency and the SPR wave vector at a metal-dielectric interface [7, 8].

In 1968, A. Otto was able to excite surface plasmon waves in a silver film using an attenuated internal reflectance scheme, illustrated in Figure 1.1(a), and for the first time recorded them [9]. In this scheme, the film is located close to the prism but does not touch it, thus creating an air gap. Otto's configuration was subsequently modified by E. Kretschmann [10], who proposed using the properties of surface plasmon waves to study thin metal films. In his scheme,

the metal film is coated on the bottom surface of the prism, as represented in Figure 1.1(b).

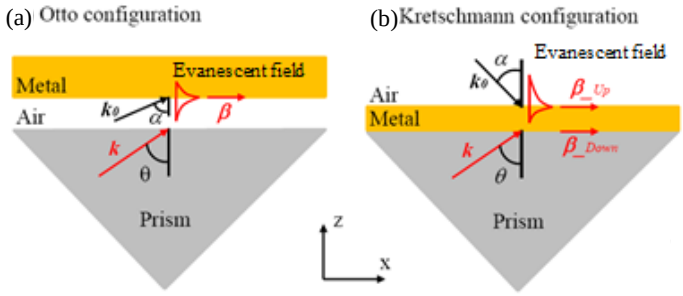

Figure 1.1: Prism coupling to excite SPRs using the attenuated total internal reflection in the (a) Otto and (b) Kretschmann configurations[11].

Effective excitation of surface plasmon waves in metal-dielectric structures leads to an emergence of several new optical phenomena, such as anomalous transmission [12] and absorption [13], optical and magneto-optical [14] activity, and plasmon focusing [15].

1.2 Types of Plasmons

In physics, a plasmon is a quantum of plasma oscillation. Just as light consists of photons, the plasma oscillation consists of plasmons. The plasmon can be considered as a quasiparticle since it arises from the quantization of plasma oscillations, just like phonons are quantizations of mechanical vibrations. Thus, plasmons are collective oscillations of the free electron gas density. At optical frequencies, plasmons can couple with a photon to create another quasiparticle called a plasmon polariton. Three possible types of plasmons can be distinguished according to the media structure, effective system size, and the presence of media boundaries: bulk plasmons, surface plasmons, and localized surface plasmons.

Bulk (or volume) plasmons exist in bulk (infinite) metals. Their physical interpretation is a collective oscillation of a free-electron gas with respect to the fixed background of positive atom cores. The quanta of this charge oscillation are called bulk plasmons. They are longitudinal oscillations of charge density. Being longitudinal waves, bulk plasmons cannot couple to transversal electromagnetic fields and thus cannot be excited through direct irradiation.

Surface plasmon resonance (SPR) is the resonant oscillation of conduction electrons at the interface between negative and positive permittivity materials

stimulated by incident light. Exactly this type of plasmon is at the basis of the majority of nanoplasmonics standard tools.

Another type of plasmons are localized SPRs (LSPRs). These are collective electron charge oscillations in metallic nanoparticles of a size comparable to or smaller than the light wavelength used for excitation. They exhibit enhanced field amplitude near the particle's surface at the resonance wavelength [16]. This field is highly localized at the nanoparticle and decays exponentially away from the nanoparticle-dielectric interface into the dielectric medium.

1.3 Surface Plasmon Resonance Nature and Conditions of Excitation

SPRs can be interpreted as electromagnetic waves trapped by the metal surface due to interactions with free electrons. The hybrid nature of the surface plasmon is reflected in its initial name: plasmon-polariton. Here, "plasmon" refers to the charge oscillations on the metal surface, and "polariton" to the electromagnetic field in the dielectric [17].

Figure 1.2 illustrates the electromagnetic field lines and the associated surface plasmon electric charge concentration at the boundary between a metal and a dielectric. The near-surface positive charge of the metal is associated with a deficiency of conduction electrons in this area, the negative one - with their excess.

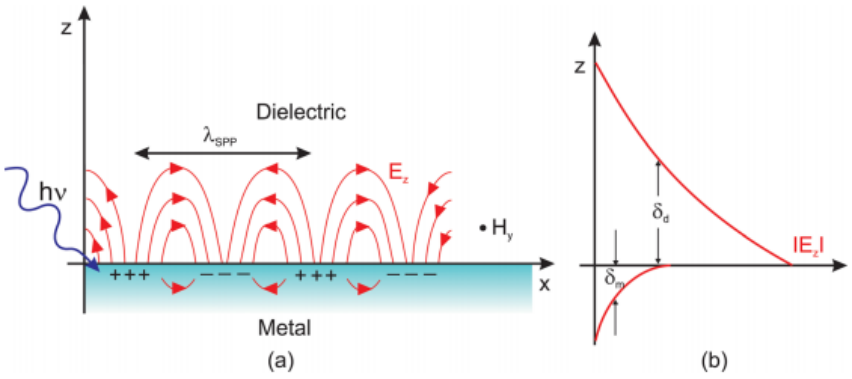

Figure 1.2: (a) Schematic illustration of electromagnetic wave and surface charges at the interface between the metal and the dielectric material, and (b) the local electric field component is enhanced near the surface and decays exponentially with distance in a direction normal to the interface [18].

It can be seen from Figure 1.2 that the magnetic field of the surface plasmon is oscillating parallel to the interface between the media and perpendicular to the plane of the figure. At the boundary, the electric field vector is normal to the interface. Positive charges are localized in the metal in the places where the electric field strength vector is directed outwards from the metal-dielectric interface, and negative charges - in the places where the electric field vector is directed towards the boundary. The electric field lines are bent in a way so as to satisfy the boundary conditions. As a result, as shown in Figure 1.2(b), the electric field decays exponentially with distance from the conductor's surface, hence the energy of the surface plasmon is concentrated near the metal-dielectric boundary. The electric field penetrates the metal until reaching its skin depth δ_m, and the dielectric - to a depth δ_d on the order of the irradiation light wavelength. Thus, the electromagnetic field strength of the surface plasmon is high near the surface (much higher than the field strength of the light wave exciting the SPR) and decays moving away from it in the direction normal to the surface. This property is widely used in nano-optics since it allows concentrating and channeling radiation using sub-wavelength structures [19].

SPRs have certain specific properties which distinguish them from ordinary spatial electromagnetic waves. The electric field of a surface plasmon is associated with an electric charge, while in a flat wave, the electric field is interdependent with the time variation of the magnetic field. Also, an SPR is a longitudinal-transverse wave. As seen in Figure 1.2, its electric field, in addition to the transverse *z*-component of the intensity, also has an *x*-component oriented along the wave vector in the direction of the plasmon propagation. SPRs are present in two environments at once: the dielectric and the conductor, while the plane wave propagates in the dielectric (a particular case is a vacuum) and the bulk plasmon - in the conductor.

A necessary condition for the existence of an SPR is a negative real part of permittivity of one of the media (metal). Also, the SPR excitation efficiency strongly depends on the optical properties of the metal, the surface morphology and relief parameters, such as the profile shape and depth, the thickness of the deposited metal layer, and random surface heterogeneity [20]. The SPR wave vector is always larger than the wave vector of an electromagnetic wave in free space. Thus, the initiation of the SPR is possible only with the help of special techniques that allow matching of the wave-vector magnitudes, i.e. to satisfy the propagation phase matching condition [19]. Some of these techniques are explained in Section 1.4.

SPR excitation becomes especially effective when the incident light is polarized and its wave vector projection onto the metal film plane is equal to the wave vector of the surface plasmon [21].

1.4 Surface Plasmon Resonance Excitation Methods

In order to excite SPR, the momentum of the incoming light must be matched to that of the surface plasmon. When the momentums are matched, an SPR is generated by coupling of an electric field with free electrons in a metal. For effective excitation of SPR, the prism method [9, 12], the excitation in metal-dielectric waveguides [22], and the methods using periodic metal gratings are most often used [23].

1.4.1 Prism Method

In the works of Otto [9] and Kretschmann [10], SPRs were excited by light passing through a prism made of a dielectric material with a high refractive index. When a light wave propagating in the prism totally reflects off the prism base, an evanescent electromagnetic wave decays exponentially in the direction perpendicular to the prism–metal interface [24]. If the metal film is sufficiently thin (less than 100 nm for light in the visible and near-infrared part of spectrum), the evanescent wave penetrates through the metal film and couples with an SPR at the outer boundary of the metal film [25]. The diagrams of the devices in both configurations were shown earlier in Figure 1.1. Due to its simplicity and high efficiency of plasmons excitation, Kretschmann's geometry is used in the majority of SPR sensors based on prism devices.

1.4.2 Waveguide Method

Due to the effect of total internal reflection, light can propagate inside an optical waveguide - a transparent channel made of a material with high refractive index. Figure 1.3 represents a planar waveguide basic scheme for the SPR excitation. The interaction between the optical waveguide modes and surface plasmon waves can be analyzed by studying the optical properties of the individual modes propagating inside the waveguide.

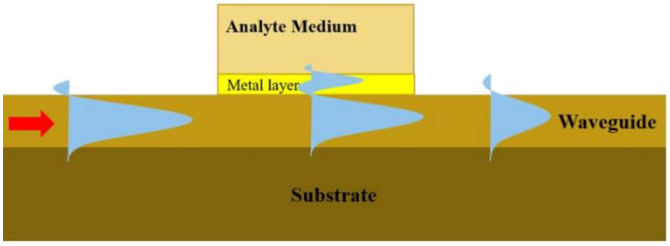

Figure 1.3: Waveguide SPR sensor scheme [26].

This SPR excitation approach can be realized in various configurations of waveguides. Most often, such SPR-systems are implemented in the form of fiber-optic channels with a metal coating on the materials' boundary [27]. Optical waveguides on glass substrates are also widely used. The advantages of glass-based waveguides are their low cost, proven technology of production and processing, and the ability to manufacture substrates of almost any given size.

1.4.3 Diffraction Gratings

One of the most interesting ways to initiate the SPR is based on the increase of the incident light-wave vector due to the diffraction of electromagnetic radiation by a diffraction grating, as depicted in Figure 1.4. In this method, the SPR is excited due to diffracted wave coupling with the surface plasmons when their propagation constants are closely phase-matched.

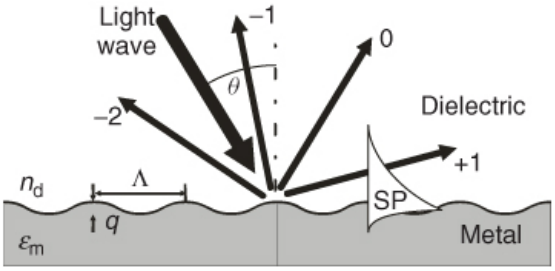

Figure 1.4: SPR excitation by the diffraction of light on a diffraction grating [25].

The resulting SPR excitation efficiency depends on the angle of incidence θ, the dielectric medium refractive index n_d, the metal grating dielectric permittivity ε_m, the grating pitch Λ, the grating depth q, and the profile shape. The prism excitation method of the SPR has a smaller number of varying parameters, which makes it simpler to implement. Also, in the case of a

diffraction grating, the efficiency of the SPR excitation can be increased by optimal selection of the grating structural parameters.

1.5 Surface Plasmon Resonance Imaging and Biosensors

The possibility of effective excitation of SPR and its influence on many photo-physical processes occurring on the surface of investigated materials prompted a wide range of applications of this phenomenon in scientific laboratories and industry. The SPR properties have a great practical value for developments in optical spectroscopy, non-linear optics, high-resolution microscopy, light modulators, biosensors technology development, and other areas. One of these areas, the SPR imaging (SPRi), also called Surface Plasmon Resonance Microscopy (SPRM), is a label-free analytical tool that combines the surface plasmon resonance of metallic surfaces with the imaging of the metallic surface [28]. For this work, the SPRM is defined as a recording of two-dimensional high-contrast real-time images obtained as a map of the local distribution of refractive index of inhomogeneous mixtures placed atop of the metallic diffraction grating.

1.5.1 Diffraction limit

Usually, the observation of Angstrom-size objects is impossible with visible light. The light diffraction phenomenon imposes a resolution limit on the microscope. The diffraction limit is the minimum value of the scattering spot size, which can be obtained by the electromagnetic radiation focusing. The diffraction limit d_{min} was discovered in 1873 by Ernst Abbe and is determined by the equation [29]:

$$d_{min} = \frac{\lambda}{2n}, \tag{1.1}$$

where λ is the light wavelength in a vacuum and n is the refractive index of the medium. Sometimes, the diffraction limit is not a linear, but an angular value, defined by the equation [30]:

$$\theta = \frac{1.22\lambda}{D}, \tag{1.2}$$

where θ is the angular resolution (in radians) and D is the optical device aperture (Rayleigh criterion, proposed in 1879). An optical microscope is not able to distinguish objects of a size smaller than the value of $\lambda/(2n\sin\Theta)$, where θ is the aperture angle. For good microscopes, θ is close to 90°, therefore, the limiting resolution is close to the diffraction limit $\lambda/(2n)$.

When light rays from two-point light sources pass through an input objective lens of a certain size, this lens represents the aperture through which the light diffracts, producing two concentric circle systems. Figure 1.5 illustrates how the light diffraction phenomenon sets a microscope's resolving power limit, that is, determines a minimum distance between two luminous points at which they would be seen in a microscope as two, rather than one.

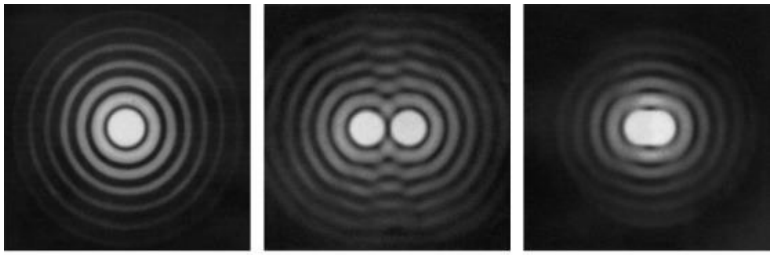

Figure 1.5: Diffraction pattern from two circular apertures: (a) pattern from a single aperture, (b) pattern from two well-separated apertures, (c) pattern from two apertures satisfying the Rayleigh criterion [31].

The diffraction theory shows that the minimum distance at which two luminous points can be distinguished from each other is about half of the wavelength at which they radiate. So, for radiation at the wavelength of 630 nm, one can count on the resolution of objects no larger than 315 nm.

1.5.2 Surface Plasmon Resonance Microscopy

In 1988, W. Knoll and B. Rothenhausler suggested using SPR for microscopy [32]. They demonstrated a working model of a microscope, in which SPRs were excited according to the Kretschmann scheme, for a study of a test sample in the form of a thin dielectric coating with well-defined periodic structure. The results turned out to be so impressive that in the next few years numerous studies on the possibility of using the device in physics, chemistry, biology, and engineering applications were carried out.

In the prism scheme, when the angle of incidence of the light beam coincides with the resonant angle of excitation of the SPR, the energy of the incident light is partially spent on the surface plasmon's excitation and the intensity of the reflected beam is lower (that is why this excitation method is often called "*the method of attenuated total reflection*"). Also, there is an optimal metal film thickness at which practically all of the energy of the incident wave is converted into the SPR energy.

Figure 1.6 depicts an SPR microscope built using the Kretschmann scheme. The prism device is illuminated by a narrow monochromatic linearly polarized light beam (the polarization vector lies in the plane of incidence of light, that is the light is p-polarized. The light reflected from the film is incident on the image sensor (element 6 in Figure 1.6) and can be processed by a computer.

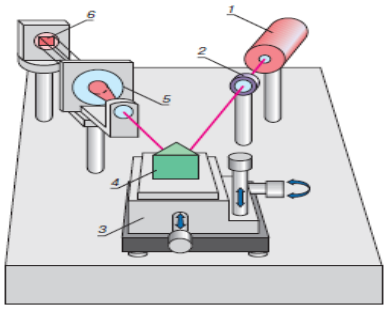

Figure 1.6: SPR Microscope Scheme: 1 – laser, 2 – polariser, 3 – position adjustment mechanism, 4 – prism with a thin metal film on its hypotenuse surface where the SPR is excited, 5 – telescope, 6 – image sensor [33].

A telescope is placed between the prism and the image sensor in order to expand the beam so that light coming from each micron-size area of the film falls on several elements of the image sensor (the image sensor pixel size is approximately on the order of ten microns).

Any thin film on the metal surface can be represented as a local change in the dielectric properties of the environment affecting the SPR excitation conditions. Therefore, when the microscope is adjusted to an angle corresponding to the optimal SPR excitation for a clean metal film, the intensity of the reflected light becomes higher in those fragments where the observed object is located. In fact, the microscope does not respond to the object's thickness only, but to changes in the parameter εd, where ε is the dielectric permittivity and d is the thickness of the object being measured. A microscope designed by this scheme was initially used to monitor monomolecular oriented films structure (so-called Langmuir-Blodgett films) [34] at the time of their formation on liquid surfaces and transferring them to solid substrates. This is one of the basic schemes of a surface plasmon microscope. There are numerous modifications that are convenient for solving specific problems.

1.5.3 Biosensors

Another area of the SPR microscopy application is direct observation of biological objects (bacteria). Their structure observation just with the visible light transition is almost impossible, that is why biologists normally use contrast fluids to observe their objects. Plasmon microscopes allow observing them without these tricks. For example, it was shown that in the aquatic environment, it is possible to distinguish the boundary between the cytoplasm and the cell membrane [28]. An SPR-based biosensor is made up of an SPR sensor and suitable surface functionalization acting as the biorecognition element. When a biomolecular interaction (e.g. specific binding of analytes) takes place, the refractive index near the surface is altered. This modification of refractive index can then be detected by the SPR sensor [35].

SPR-based biosensors were first launched into production by Pharmacia Biosensor AB (Sweden) in 1990 [36]. At the beginning of their development, SPR sensors were very expensive, so the task of developing low cost highly sensitive SPR systems was quite topical for a long time. At present, with the advent of new fabrication technologies, SPR-based biosensors are widely used in the pharmaceutical industry and in research laboratories.

Most of the existing SPR biosensors are built using the Kretschmann prism scheme, as depicted in Figure 1.7, where the intensity of the reflected light depends on the excitation efficiency of SPR and therefore correlates with the refractive index spatial distribution near the metal film surface. In a typical SPR biosensing experiment, one interactant in the interactant pair i.e., a ligand or biomolecule, is immobilized on an SPR-active gold-coated glass prism and the other interactant in an aqueous buffer solution is induced to flow across this surface as depicted in Figure 1.7. When light is shined through the glass prism and onto the gold surface at angles and wavelengths near the so-called “surface plasmon resonance” condition, the optical reflectivity of the gold changes very sensitively with the presence of biomolecules on the gold surface or in a thin coating on the gold. The extent of binding between the solution-phase interactant and the immobilized interactant is easily observed and quantified by monitoring this reflectivity change.

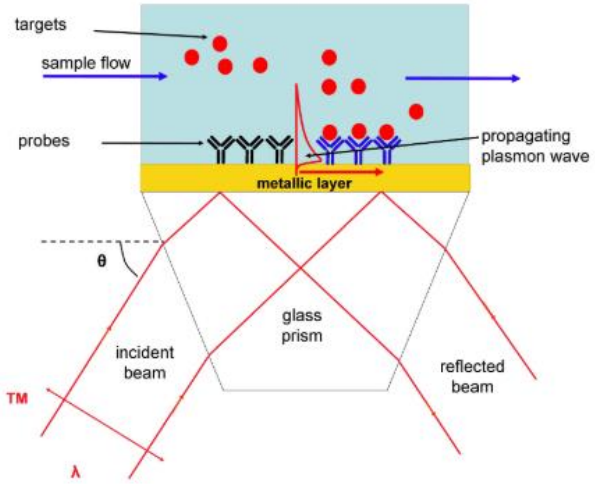

Figure 1.7: Diagram of a typical SPR biosensor system. The transverse magnetic (TM)–polarized incident beam of wavelength λ is refracted through a high-index glass prism of angle ϑ [37].

Another class of existing SPR sensors are sensors based on metal diffraction gratings, shown in Figure 1.8. These optical elements reduce the size of the sensors. Grating-based SPR sensor fabrication cost can also be kept low using the fabrication procedure developed at RMC. In addition, sensors of this type do not need a fluid with a specific refractive index to create an optical contact between the prism and the SPR chip. An SPR sensor based on a polymer grid covered with a gold film was created in 2001 [38]. The sensor element was illuminated with monochromatic radiation, and the reflected radiation, carrying information about the spatial distribution of the SPR intensities in the chip, was recorded using a CCD array.

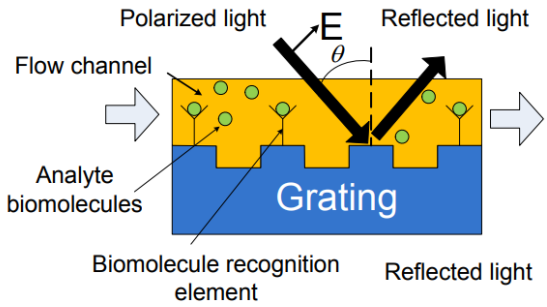

Figure 1.8: Schematics of grating-based SPR biosensor [39].

In a traditional SPR system, an average intensity of the reflected light from an entire surface is measured and results are represented as average refractive

index variations of a sample on the entire surface. In SPR imaging (SPRi), the intensity of the reflected light is analyzed at each position on the sensing surface. The output of this sensor is a grey-scale image, which is called a difference image and represents refractive index changes of the dielectric media above the metal film pixel by pixel.

After the discovery at RMC in the 1990's of the surface relief diffraction grating fabrication method using optical alteration of an azoaromatic polymer film [40], extensive studies of the potential application of this method have been conducted in our group, with some of those studies leading to the creation of an SPR sensor working in transmission mode [41] and, more recently, an E. Coli bacteria detector based on plasmonic crossed surface relief grating (CSRG) [42].

1.6 Diffraction Gratings

A diffraction grating is an optical element with a periodic structure that can influence the light-wave propagation so that the energy of the wave that has passed through the grid or reflected from it is concentrated in certain directions. The directions of propagation of these beams depend on the period of the grid and the incident light wavelengths, that is, the diffraction grating operates as a dispersion element.

1.6.1 Principle of Operation

The principle of operation of a diffraction grating is based on the diffraction of the light waves that interact with it and the subsequent interference of these diffracted waves. In the general case, the diffraction grating can be represented as a set of parallel and equidistant transparent slits separated by identical opaque spaces. The slits' width and the distance between them are on the order of the light wavelength. When a light beam passes through such a grid, any point of each slit will act as a secondary light source. Figure 1.9 illustrates the diffraction scheme of a plane wave.

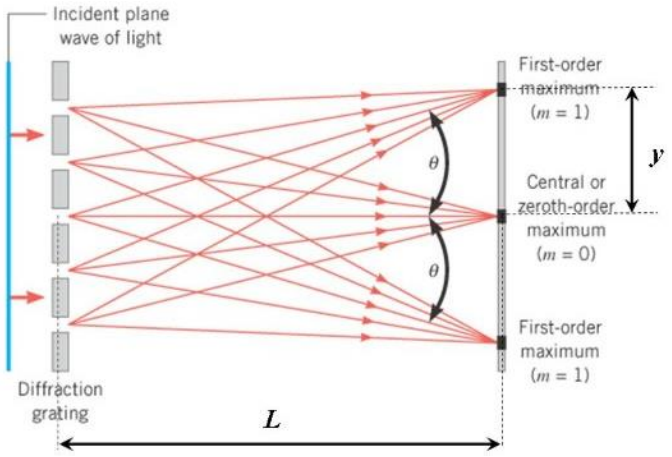

Figure 1.9: Plane wave diffraction scheme [43].

The light waves from different grating slits interfere with each other. If these waves are in the same phase, then they amplify each other. In other words, constructive interference occurs. If the waves are in the antiphase, then they are extinguished, that is, destructive interference takes place. The propagation directions of the diffracted waves, on which the constructive interference occurs, are called diffraction maxima. These maxima are designated by integers, which are called diffraction orders (m). The number of diffraction maxima and their propagation directions depend on the period of the grating and the light wavelength and can be determined by the diffraction grating equation [44]:

$$\Lambda(\sin\theta_m - \sin\theta_i) = m\lambda\,, \tag{1.3}$$

where Λ is the grating elements' spacing (grating pitch), θ_m is the diffracted angle of light, θ_i is the angle between the diffracted ray and the grating's normal vector, m is an integer representing the propagation mode of interest (the diffraction order), and λ is the incident light wavelength. From this equation, it follows that the diffraction angle depends on the wavelength of light. Therefore, if white light is shone on a grating, it will be decomposed into a spectrum.

1.6.2 Diffraction Gratings Brief History

Periodic gratings have always been of great interest because of their ability to decompose light into a spectrum, which has made them a powerful analytical tool for physicists. The diffraction phenomenon was discovered a long time ago,

but the first hand-made diffraction grating was produced in 1785 by American astronomer D. Rittenhouse [45]. He made it from parallel hairs that were mounted in a frame on the lens of his telescope in order to obtain a spectrum of stars.

At the end of 19th century G. A. Rowland, Professor of Physics at Johns Hopkins University, designed a series of engraving machines for diffraction gratings cutting with a period of up to 1.5 μm and a size of up to 18 cm. He also produced the first diffraction gratings on spherical surfaces that simultaneously performed the role of a grating and a focusing lens.

In 1948, the future Nobel laureate D. Gabor proposed the method of optical holography - a method of recording, reproducing and transforming wave fields based on interference and diffraction of light waves. In the 1960s, after the invention of the laser, the manufacturing technology of holographic diffraction gratings was developed. It was based on the method of recording interference patterns from laser radiation. The registration was carried out by a photosensitive material deposited on a substrate. Depending on the material, a periodic diffraction structure may be obtained resulting from the material surface shape alteration caused by the irradiation or through its subsequent chemical treatment. Then, the obtained relief is covered with a thin metal film. This technology allows obtaining not only strictly periodic gratings but also gratings with variable pitch, as well as various two- and even three-dimensional patterns [46-48].

1.7 Azobenzene Films

In the 1990s, Rochon, Batalla, and Natansohn [40] found that the simplest aromatic azobenzene compound can be used as a material for the surface relief grating (SRG) fabrication due to its unique photo-isomerization properties. Composed of two phenyl rings linked by a nitrogen double bond, azobenzene has two isomers: the *trans*-form and the *cis*-form, as shown in Figure 1.10. The transition of a molecule from one form to another is possible as a result of interaction with light. The transition from *trans* to *cis* happens when azobenzene is irradiated by light at wavelengths in the *trans*-isomer absorption band. The back-relaxation takes place in dark or under irradiation at wavelengths in the *cis*-isomer absorption band [49].

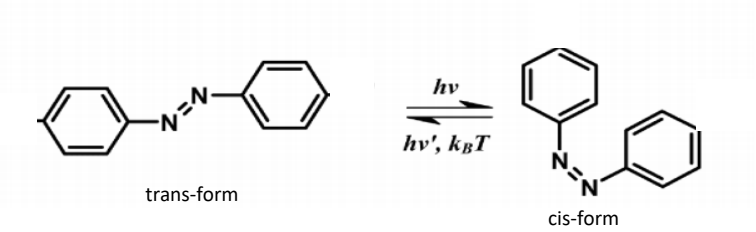

Figure 1.10: The photo-isomerization cycle for azobenzene [50].

This azobenzene molecules' reaction to light irradiation results in light-induced molecular motion [51]. This motion occurs in such a way that a localized mass transfer happens from higher light intensity areas towards regions with low-intensity irradiation [40]. For example, if an azobenzene film is irradiated by a linear interference pattern, this pattern will be imprinted onto the film surface creating a sinusoidal surface profile.

Although the *cis*-isomer relaxes back to the stable *trans*-isomer, the imprinted pattern keeps its shape which remains stable under ambient conditions up until the azobenzene glass transition temperature, which is 69 °C. Thus, the obtained relief can be used for subsequent metal coating and diffraction grating fabrication. The ability of azobenzene to keep its shape allows subsequent irradiation with light of different interference patterns, thereby obtaining specific diffraction grating patterns [46-48].

1.8 Thesis Statement

The goal of this thesis is to use the SPRM for the imaging of inhomogeneous liquid mixtures. This study is based on the fact that the refractive index changes resulting from the mixture inhomogeneity can be captured with a camera after a polarized light beam passed through a layer of the mixture and an SPR device. Unlike the conventional SPR sensing, where data are averaged over the sensing area, the SPRM produces SPR intensity variation data at each pixel of the image, offering spatial mapping of any given sensing area and much more information.

The SPR device fabrication technique is based on the direct laser interference patterning method applied on azobenzene molecular glass films using a Lloyd's mirror interferometer [52]. The device is fabricated in a crossed surface relief grating shape by orthogonal superposition of two periodic sinusoidal gratings covered by a 60-nm silver film. The grating parameters (pitch and depth) are chosen in such a way that the SPR conversion occurs when the sample is irradiated by monochromatic light of 632 nm wavelength. In the imaging setup, polarized light passes through the SRG and the examined media

(inhomogeneous liquid mixture) located on the SRG in a polydimethylsiloxane (PDMS) well covered by a cover glass. Then the light signal is registered by a camera.

Two types of light sources were used in this study: a coherent light beam from a He-Ne laser and a white halogen lamp light filtered at 632 nm wavelength by a narrowband interference filter. Different types of inhomogeneous aqueous mixtures were imaged during the experiments: mineral oil mixed with deionized water, silicon oil mixed with deionized water, and silica gel particles mixed with deionized water. Different types of mixture components were utilized in order to provide a variety of mixture behaviour in contact with the SRG as well as to use mixture components with different refractive indices.

In this thesis, the results of imaging made with a CCD high-dynamic range 762x576 pixel camera are shown in both still pictures and video formats. Also, experimental attempts for understanding the SPR propagation are made by comparing images of scratches and light-blocking objects on the metallic grating surface.

1.9 Structure of the Thesis

This thesis consists of five main parts. Chapter 1 briefly introduces the SPR phenomenon, its physical nature, and conditions of excitation. It goes on to explain the main SPR excitation methods and applications based on this phenomenon in modern physics and engineering.

Chapter 2 contains an overview of the theoretical concepts and ideas relevant to the SPR theory, starting with the electromagnetic nature of light, described by Maxwell's equations leading to an analytical description of the SPR dispersion relation. Finally, surface plasmon polarization conversion in CSRG is explained.

Chapter 3 details the experimental processes for sample fabrication and describes the experimental equipment and procedures used for sample analysis.

Chapter 4 presents the results of the experiments. It provides the SRG optimization procedure results, followed by the analysis and comparison of different measurement results and presents the images and videos obtained during the experiments.

Finally, Chapter 5 summarizes the results shown previously, outlines the work to be done and concludes the thesis.

2 Theoretical Overview

2.1 Maxwell's Equations and Electromagnetic Waves Propagation

By the middle of the 19th century, when it had become clear that light and electromagnetic fields were one and the same, a mathematical instrument in the form of Maxwell's equations was developed for relating the electric and magnetic fields changing in time and space. These equations were the result of intensive studies of electricity, magnetism and light propagation. Formulated by James Clerk Maxwell on the basis of experimental results accumulated in the first half of the 19th century, these equations played a key role in the development of theoretical physics. They had a strong, often decisive, influence on all areas of physics directly related to electromagnetism (and many others), including the understanding of light as an electromagnetic wave. In essence, all the theoretical substantiation of optical phenomena used in the research being presented in this thesis and described further in this chapter can be derived from the following Maxwell's equations in their differential form [53]:

$$\nabla \cdot \boldsymbol{E} = \frac{\rho}{\varepsilon_0 \varepsilon_r} \tag{2.1}$$

$$\nabla \cdot \mu_0 \mu_r \boldsymbol{H} = 0 \tag{2.2}$$

$$\nabla \times \boldsymbol{E} = -\mu_0 \mu_r \left(\frac{\partial \boldsymbol{H}}{\partial t}\right) \tag{2.3}$$

$$\nabla \times \boldsymbol{H} = \boldsymbol{J} + \varepsilon_0 \varepsilon_r \left(\frac{\partial \boldsymbol{E}}{\partial t}\right), \tag{2.4}$$

where $\boldsymbol{E}$ is the electric field vector, ρ - the volume charge density, ε_0 - the free space permittivity, ε_r – the relative permittivity of the medium, μ_0 – the free space permeability, μ_r – the relative permeability of the medium, $\boldsymbol{H}$ – the magnetic field vector, and $\boldsymbol{J}$ is the current density.

In a charge-free and current-free space (i.e. a vacuum), Maxwell's Equations 2.1-2.4 simplify to the following form:

$$\nabla \cdot \varepsilon_0 \boldsymbol{E} = 0 \tag{2.5}$$

$$\nabla \cdot \mu_0 \boldsymbol{H} = 0 \tag{2.6}$$

$$\nabla \times \boldsymbol{E} = -\mu_0 \left(\frac{\partial \boldsymbol{H}}{\partial t}\right) \tag{2.7}$$

$$\nabla \times \boldsymbol{H} = \varepsilon_0 \left(\frac{\partial \boldsymbol{E}}{\partial t}\right). \tag{2.8}$$

In Maxwell's theory, for the first time, two fundamental interactions, electric and magnetic, previously considered independent, were combined and the notion of the *electromagnetic* field came into use.

An electromagnetic wave manifests itself as an electromagnetic field propagating in free space or in materials, in which the electric and magnetic fields vary periodically. Maxwell's equations are first-order differential equations in spatial coordinates and time. However, both Equations 2.7 (Faraday's law) and 2.8 (Ampere's law) include unknown vector functions $\boldsymbol{E}$ and $\boldsymbol{H}$. Applying the curl operator to Equations 2.7 and 2.8 and using appropriate vector identity rules, the equations for $\boldsymbol{E}$ and $\boldsymbol{H}$ can be cast into second-order differential equations [53], called the Helmholtz equations:

$$\nabla^2 \boldsymbol{E} = \mu_0 \varepsilon_0 \frac{\partial^2 \boldsymbol{E}}{\partial t^2} \tag{2.9}$$

$$\nabla^2 \boldsymbol{H} = \mu_0 \varepsilon_0 \frac{\partial^2 \boldsymbol{H}}{\partial t^2} \tag{2.10}$$

Considering that a three-dimensional wave equation can be written as [53]

$$\nabla^2 f = \frac{1}{v^2} \frac{\partial^2 f}{\partial t^2}, \tag{2.11}$$

one can see that Equations 2.9 and 2.10 imply that the electromagnetic wave in a non-magnetic medium propagates with the velocity

$$v = \frac{1}{\sqrt{\mu_0 \varepsilon_0}} = c, \tag{2.12}$$

where $c = 3 \times 10^8 \, m/s$ is the speed of light in a vacuum.

One of the most important types of electromagnetic radiation is a monochromatic plane wave, in which the radiation has a planar wavefront moving in a specific direction and only one frequency component is present. The importance of this type of wave is that their mathematical description allows deriving the basic properties of a monochromatic laser. For a plane electromagnetic wave propagating along the x direction, the electric and magnetic fields can be described by sinusoidal functions as follows [53]:

$$\boldsymbol{E}(x,t) = \boldsymbol{E}_0 e^{i(\boldsymbol{k}x-\omega t)} \quad 2.13$$

$$\boldsymbol{H}(x,t) = \boldsymbol{H}_0 e^{i(\boldsymbol{k}x-\omega t)} \quad 2.14$$

where $\boldsymbol{E}_0$ and $\boldsymbol{H}_0$ are the field amplitudes, $\boldsymbol{k}$ is the wave vector, and ω is the angular frequency. Figure 2.1 illustrates the electric and magnetic fields oscillations for a monochromatic wave.

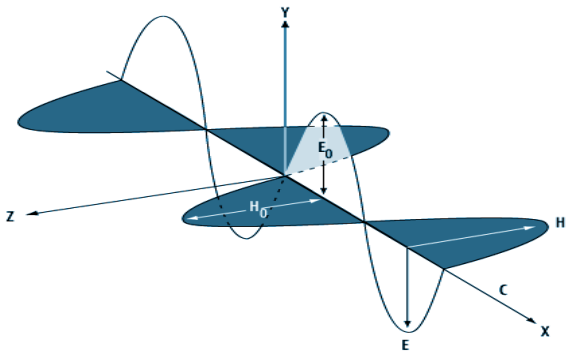

Figure 2.1: Oscillations of electric and magnetic fields in a plane electromagnetic wave [54].

Substituting Equations 2.13 and 2.14 into Maxwell's equations, one can obtain:

$$\mathbf{k}\cdot\boldsymbol{E} = 0, \quad \mathbf{k}\cdot\mathbf{H} = 0, \quad \mathbf{k}\times\mathbf{E} = \omega\mu\boldsymbol{H} \quad v^2\mu\cdot\boldsymbol{k}\times\boldsymbol{H} = -\omega\boldsymbol{E} \quad 2.15$$

where $v = \omega/k$ is the wave velocity. From these equations, it follows that both vectors $\boldsymbol{E}$ and $\boldsymbol{H}$ are orthogonal to the wave vector $\boldsymbol{k}$ and to each other, therefore, the wave is transversal.

2.2 Surface Plasmon Dispersion Relation

Recall that SPR is a resonance condition that occurs when electromagnetic radiation encounters a metal-dielectric interface under certain conditions. This electromagnetic radiation, coupled into the SPR, causes a free electron density fluctuation in the metal. Assuming harmonic time dependence $e^{-i\omega t}$ for $\boldsymbol{E}$ and $\boldsymbol{H}$, Maxwell's Equations 2.1-2.4 can be rewritten as follows [53]:

$$\nabla \cdot \varepsilon \boldsymbol{E} = 0 \tag{2.16}$$

$$\nabla \cdot \mu \boldsymbol{H} = 0 \tag{2.17}$$

$$\nabla \times \boldsymbol{E} = i\omega\mu \boldsymbol{H} \tag{2.18}$$

$$\nabla \times \boldsymbol{H} = -i\omega\tilde{\varepsilon}\boldsymbol{E}, \tag{2.19}$$

where

$$\varepsilon = \varepsilon_0 \varepsilon_r \tag{2.20}$$

$$\mu = \mu_0 \mu_r \tag{2.21}$$

$$\tilde{\varepsilon} = \tilde{\varepsilon}' + i\tilde{\varepsilon}'', \tag{2.22}$$

Here $\tilde{\varepsilon}$ is the complex permittivity of a material. Its real part $\tilde{\varepsilon}'$ caracterises a material's ability to store electrical energy, whereas its imaginary part serves as a measure of electric field dissipation in a material.

For describing the SPR propagation along a metal-dielectric boundary, Maxwell's Equations 2.16-2.19 must be solved separately for two different regions. The geometry of an interface between a metal (y $<$ 0, with a complex permittivity $\tilde{\varepsilon}_m$) and a dielectric ($y > 0$, with only a real permittivity ε_d) is represented in Figure 2.2 for a TM-polarized incident wave on a diffraction grating.

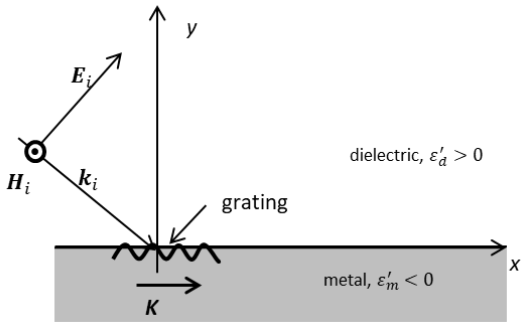

*Figure 2.2: Metal-dielectric boundary and a light wave incident on a grating with the grating vector **K** parallel to the x- component of the electric field vector **E_i**.*

Assuming that the SPR wave propagates in the *x*-direction and decays in the y-direction, its wave vector can be mathematically described as follows:

$$\boldsymbol{k} = k_x + ik_y \,, \tag{2.23}$$

with its x-component being real and the y-component being imaginary. Hence, the SPR dispersion relation can be developed if the expressions for k_x and k_y are obtained.

For the TM-polarized wave incident on a grating, as represented in Figure 2.2, the complex fields can be described by the following expressions:

$$\boldsymbol{E}_d = \left(E_{x,d}, E_{y,d}, 0\right) e^{i\left(k_{x,d}x + k_{y,d}y\right)} \tag{2.24}$$

$$\boldsymbol{H}_d = \left(0,0, H_{z,d}\right) e^{i\left(k_{x,d}x + k_{y,d}y\right)} \tag{2.25}$$

in the dielectric ($y > 0$) and

$$\boldsymbol{E}_m = \left(E_{x,m}, E_{y,m}, 0\right) e^{i\left(k_{x,m}x + k_{y,m}y\right)} \tag{2.26}$$

$$\boldsymbol{H}_m = \left(0,0, H_{z,m}\right) e^{i\left(k_{x,m}x + k_{y,m}y\right)} \tag{2.27}$$

in the metal ($y < 0$), where the subscripts m and d denote the metal and the dielectric, respectively.

For linear, non-magnetic ($\mu_r = 1$) materials, the general boundary conditions for the case depicted in Figure 2.2 are defined as [53]:

$$E_{x,m} = E_{x,d} \quad 2.28$$

$$H_{z,m} = H_{z,d} \quad 2.29$$

$$\varepsilon_m E_{y,m} = \varepsilon_d E_{y,d} \quad 2.30$$

Inserting Equations 2.24-2.27 into Maxwell's Equation 2.19 and applying the curl operator in the obtained equations, one gets:

$$\left(ik_{y,d}H_{z,d}, -k_{x,d}H_{z,d}, 0\right) = \left(-i\omega\varepsilon_d E_{x,d}, -i\omega\varepsilon_d E_{y,d}, 0\right) \quad 2.31$$

$$\left(ik_{y,m}H_{z,m}, -k_{x,m}H_{z,m}, 0\right) = \left(-i\omega\tilde{\varepsilon}_m E_{x,m}, -i\omega\tilde{\varepsilon}_m E_{y,m}, 0\right) \quad 2.32$$

Equating the corresponding spatial vector components yields the following equations:

$$ik_{y,d}H_{z,d} = -i\omega\varepsilon_d E_{x,d} \quad 2.33$$

$$ik_{y,m}H_{z,m} = -i\omega\tilde{\varepsilon}_m E_{x,m} \quad 2.34$$

$$-k_{x,d}H_{z,d} = -i\omega\varepsilon_d E_{y,d} \quad 2.35$$

$$-k_{x,m}H_{z,m} = i\omega\tilde{\varepsilon}_m E_{y,m}, \quad 2.36$$

Applying the boundary conditions established in Equations 2.28-2.30 to Equations 2.33-2.36, one gets

$$k_{x,d} = k_{x,m} \equiv k_x \quad 2.37$$

$$\frac{k_{y,d}}{\varepsilon_d} = \frac{k_{y,m}}{\tilde{\varepsilon}_m} \quad 2.38$$

Using the dispersion relation of light $k = \omega/v$ [53] for a wave propagating with the velocity $v = 1/\sqrt{\mu\varepsilon}$, the following equation can be obtained:

$$k^2 = \omega^2\mu\varepsilon\,, \quad 2.39$$

Taking into account the equality obtained in Equation 2.37, Equation 2.39 yields:

$$k_d^2 = k_x^2 + k_{y,d}^2 = \omega^2\mu_d\varepsilon_d \quad 2.40$$

$$k_m^2 = k_x^2 + k_{y,m}^2 = \omega^2 \mu_m \tilde{\varepsilon}_m \tag{2.41}$$

Finally, combining Equations 2.38, 2.40, and 2.41 and solving the system of equations for k_x for non-magnetic media ($\mu_m = \mu_d = \mu_0$), one obtains the SPR dispersion relation as follows:

$$k_{sp} = k_x = \frac{\omega}{c}\sqrt{\frac{\varepsilon_{r,d}\tilde{\varepsilon}_{r,m}}{\varepsilon_{r,d} + \tilde{\varepsilon}_{r,m}}} = k_x' + ik_x'' \,, \tag{2.42}$$

where the subscript r denotes the relative permittivity and $c = 1/\sqrt{\varepsilon_o \mu_0}$ is the speed of light in a vacuum.

It can be noted that the SPR dispersion relation 2.42 was obtained for a flat interface assumption, therefore, the grating modulation depth is considered small. If the grating is too deep, plasmonic band gaps can be present, which are unaccounted for in the theory. However, this theory can serve as a good approximation of the SPR wavenumber for sinusoidal gratings with depths smaller than the SPR propagation length.

Using the obtained expression for k_x, Equations 2.40 and 2.41 can be solved for k_y in both media:

$$k_{y,d} = \pm\frac{\omega}{c}\sqrt{\frac{\varepsilon_{r,d}^2}{\varepsilon_{r,d} + \tilde{\varepsilon}_{r,m}}} = k_{y,d}' + ik_{y,d}'' \,, \tag{2.43}$$

$$k_{y,m} = \pm\frac{\omega}{c}\sqrt{\frac{\tilde{\varepsilon}_{r,m}^2}{\varepsilon_{r,d} + \tilde{\varepsilon}_{r,m}}} = k_{y,m}' + ik_{y,m}'' \,, \tag{2.44}$$

Recall that metals are not perfect conductors and their complex electrical permittivity consists of real and imaginary parts:

$$\tilde{\varepsilon}_{r,m} = \tilde{\varepsilon}_{r,m}' + i\tilde{\varepsilon}_{r,m}'' \tag{2.45}$$

Using this form in the obtained SPR dispersion relations 2.42-2.44, the real parts of the wave vector components can be found [55]:

$$k_{sp}' = k_x' \cong \frac{\omega}{c}\sqrt{\frac{\varepsilon_{r,d}\tilde{\varepsilon}_{r,m}'}{\varepsilon_{r,d} + \tilde{\varepsilon}_{r,m}'}} \tag{2.46}$$

$$k'_{y,d} \cong \frac{\omega}{c}\sqrt{\frac{\varepsilon'^{2}_{r,d}}{\varepsilon_{r,d}+\tilde{\varepsilon}'_{r,m}}} \quad 2.47$$

$$k'_{y,m} \cong \frac{\omega}{c}\sqrt{\frac{\varepsilon'^{2}_{r,m}}{\varepsilon_{r,d}+\tilde{\varepsilon}'_{r,m}}} \quad 2.48$$

The evanescent nature of the SPR wave propagating along the boundary requires that the component k'_x must be real whereas the component normal to the interface $k'_{y,i}$ $(i = m, d)$ must be imagimary. Since the permittivity of the dielectric $\varepsilon_{r,d}$ is real and positive, Equations 2.46-2.48 impose the following conditions for the real part of the permittivity of the metal for the bound SPR excitation at a metal-dielectric interface:

$$\tilde{\varepsilon}'_{r,m} < 0 \quad 2.49$$

$$\tilde{\varepsilon}'_{r,m} < -\varepsilon_{r,d} \quad 2.50$$

2.2.1 Dispersion Relation and Drude Model

The Drude model is often used to describe the kinetic properties of electrons in materials. This model assumes that a conductive material consists of a lattice of immobile positive ions with free electrons moving through the lattice. These free electrons, like gas atoms in the kinetic theory, are considered as identical solid spheres that move along straight lines until they collide with each other or with the lattice ions. It is assumed that the duration of an individual collision is negligible and that no other forces act between them except those arising at the moment of collision. The Drude model leads to the following expression for the real part of the relative permittivity of metals [19]:

$$\tilde{\varepsilon}'_{r,m} = 1 - \frac{\omega_p^2 \tau^2}{\omega^2 + \tau\omega} \quad 2.51$$

where ω_p is the bulk plasma frequency of the metal and τ is the mean time between electron collisions in the metal. The plasma frequency is given by [56]

$$\omega_p = \sqrt{\frac{n_e e^2}{\varepsilon_0 m_e}} \tag{2.52}$$

where n_e is the conduction electron density, e is the elementary charge, and m_e is the electron mass. For optical frequencies, when $\tau\omega \gg 1$, the real part of the metal permittivity becomes [56]:

$$\tilde{\varepsilon}'_{r,m} \approx 1 - \frac{\omega_p^2}{\omega^2} \tag{2.53}$$

Also, for optical frequencies $\omega \ll \omega_p$, therefore, the dielectic permittivity becomes negative and the first SPR excitation condition in Equation 2.49 is satisfied. Also, substituting the obtained expression for the dielectric permittivity into the second SPR excitation condition 2.50, one can get [21]:

$$\omega_{sp} = \frac{\omega_p}{\sqrt{1+\varepsilon_d}} = \omega_{max}\,, \tag{2.54}$$

which is known as the characteristic plasmon frequency [57].

The SPR dispersion relation in Equation 2.46 for a Drude metal [58] is illustrated in Figure 2.3. As shown previously, electromagnetic waves propagate at a velocity $v = \frac{1}{\sqrt{\mu_0 \varepsilon_0 \varepsilon}}$ in non-magnetic materials. The light angular frequency in a dielectric is related to the wavenumber using the following equation [53]:

$$\omega = vk \tag{2.55}$$

This is known as the linear (or light line) dispersion relation, illustrated in Figure 2.3 as a straight line.

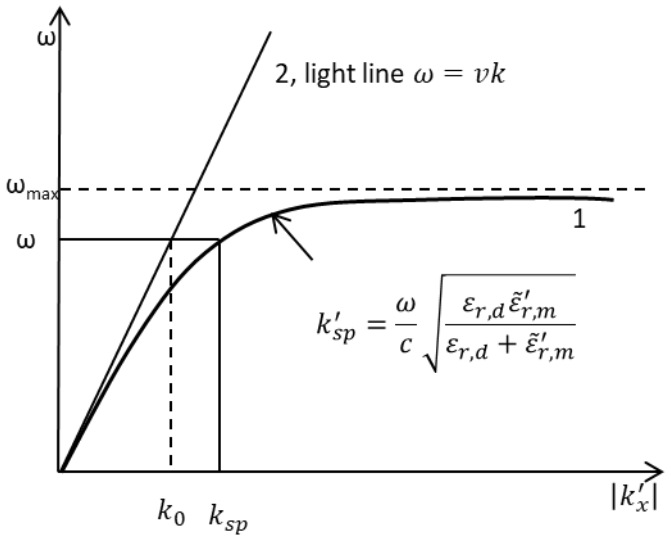

Figure 2.3: 1- SPR dispersion curve; 2- light line $\omega = vk$ [59].

The SPR dispersion relation is different from that of the light line dispersion relation due to the SPR's existence in two media simultaneously. One can see that for small values of the wave vector, the SPR dispersion curve 1 is close to the light dispersion line 2, but the curve never touches the straight line and the SPR wave vector k_{sp} is always larger than the light wave vector k_0 in free space at the same frequency. As the wave vector increases, the SPR dispersion curve bends down from the straight light line and converges to ω_{max} at infinity. This happens due to the metal permittivity frequency-dependence as seen from Equations 2.51-2.53. Therefore, additional momentum must be given to the incident light in order to excite the SPR. This extra momentum can come from the evanescent wave in the case of the Otto and Kretschmann configurations, or a diffraction grating can be used.

2.2.2 Surface Plasmon Excitation using Gratings

As explained in the introduction, there are several basic methods of the SPR excitation and one of them, the diffraction grating method, was used in this thesis. In this method, the SPR excitation is based on the wave vector increase (or light momentum increase) when the incident light encounters the grating surface. To understand this phenomenon, the grating equation must be explained first. In optics, a diffraction grating is an optical device with a regular array of diffracting elements having a size on the same order as the light wavelength, which diffracts the light into several orders that travel in different directions. The directions of these light beams depend on the spacing of the

array elements and the wavelength of the incident light. Hence, the grating acts as a dispersive element.

The grating equation can be developed for an ideal grating made up of a set of slits of spacing Λ. Assuming a plane wave of monochromatic light of wavelength λ with an angle of incidence θ_i, as illustrated in Figure 2.4, each slit in the grating acts as a quasi-point-source from which light propagates in all directions. After light interacts with the grating, the diffracted light is composed of the sum of interfering wave components emanating from each slit in the grating. At any given point in space through which diffracted light may pass, the distance to each slit in the grating varies. Since the path length varies, so does the phase of each wave. Thus, the combination of all waves will add or subtract from each other creating peaks and valleys through constructive and destructive interference.

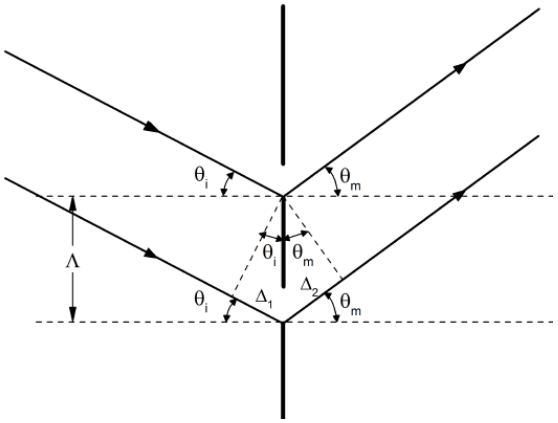

Figure 2.4: Grating slits illuminated by light incident at an angle θ_i [44].

From Figure 2.4, it can be seen that the net path length difference for waves from neighboring slits is equal to

$$\Delta = \Delta_1 + \Delta_2 = \Lambda \sin\theta_i + \Lambda \sin\theta_m, \qquad 2.56$$

where θ_m is the angle between a normal to the grating and a diffracted ray. For constructively interfering rays, the path difference should be an integer multiple of the wavelength of the incident light $\Delta = m\lambda$ and the grating equation becomes

$$\Lambda(\sin\theta_i + \sin\theta_m) = m\lambda, \quad m = 0 \pm 1, \pm 2, \ldots \qquad 2.57$$

Here, the 0th order corresponds to the direction that light would propagate if the grating was not there. For all other orders, a sign convention for the angles has to be adopted. As depicted in Figure 2.5, for the rays diffracted counterclockwise from the incident direction the orders are negative, for the clockwise diffracted rays – positive. This equation is applicable to any type of diffraction grating [44].

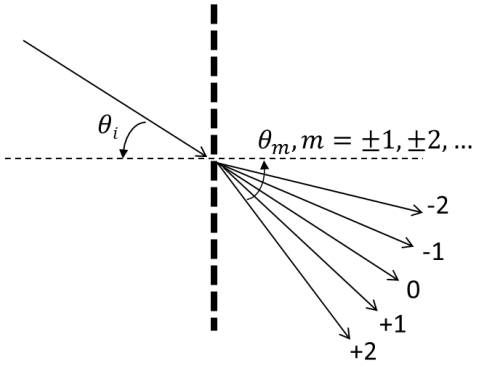

Figure 2.5: Grating diffraction orders for transmitted light.

The grating Equation 2.57 can be written in terms of the wave vector $k = 2\pi/\lambda$ as follows:

$$k \sin\theta_m = k \sin\theta_i \pm \frac{2\pi m}{\Lambda} \qquad 2.58$$

The value $2\pi/\Lambda$ is known as a magnitude of a grating vector $\boldsymbol{K}$**,** which has a direction perpendicular to the grating grooves. To increase the light momentum using a linear grating, the diffracted light wave vector projection on the plane of the grating-dielectric interface $k_{x,light}$ must be matched with the SPR wave vector k_{sp} , i.e. the phase-matching condition must be fulfilled [60]:

$$k_{x,light} = k'_{sp} \qquad 2.59$$

But the diffracted light wave vector x-component $k_{x,light}$ is equivalent to $k \sin\theta_m$ in Equation 2.58. Therefore,

$$k'_{sp} = k \sin\theta_i \pm \frac{2\pi m}{\Lambda}, \qquad 2.60$$

The sign "$\pm$" in this equation demonstrates that forward and backward diffraction can occur on the grating. In the dispersion curve, it can be illustrated in Figure 2.6.

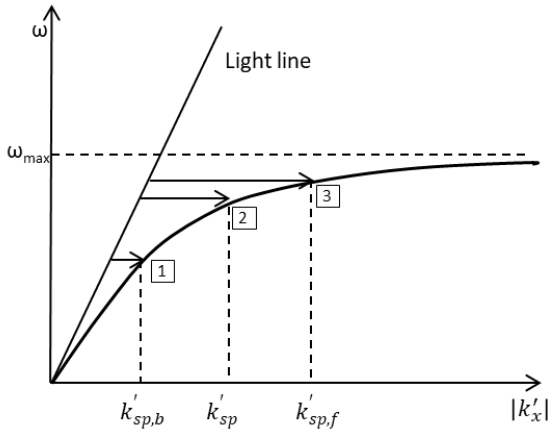

Figure 2.6: Forward and backward scattering propagation constants absolute values.

The first point on the curve corresponds to the backward diffraction for the first diffraction order $m = -1$, when

$$k'_{sp,b} = k \sin\theta - \frac{2\pi}{\Lambda}. \tag{2.61}$$

The third point corresponds to the forward scattering for the first diffraction order $m = +1$:

$$k'_{sp,f} = k \sin\theta + \frac{2\pi}{\Lambda}. \tag{2.62}$$

In this research, all experiments were carried out with the normal light incident and the second point corresponds to this case, when

$$k'_{sp} = \frac{2\pi}{\Lambda}. \tag{2.63}$$

Combining Equation 2.63 and the dispersion relation 2.46, the following equation can be obtained:

$$k'_{sp} = \frac{2\pi}{\Lambda} = \frac{\omega}{c}\sqrt{\frac{\varepsilon_{r,d}\tilde{\varepsilon}'_{r,m}}{\varepsilon_{r,d} + \tilde{\varepsilon}'_{r,m}}}. \tag{2.64}$$

Substituting the relationship between the relative permittivity and the refractive index, $n_d = 1/\sqrt{\varepsilon_{r,d}}$, and the expression for the wave vector in a vacuum, $k_0 = \omega/c = 2\pi/\lambda_0$, into Equation 2.64, an expression for the normal incident light wavelength required for the SPR excitation can be found:

$$\lambda_0 = \lambda_{sp} = n_d \Lambda \sqrt{\frac{\varepsilon_m}{n_d^2 + \varepsilon_m}}. \qquad 2.65$$

This expression is of particular importance since it establishes the relation between the dielectric medium refractive index and the SPR wavelength, thus allowing the calculation of the SPR wavelength. If the dielectric refractive index is changed, while the other conditions (the grating pitch and the type of the metal used for the grating coating) remain unchanged, the SPR wavelength shift can be calculated using Equation 2.65. This equation was also used for calculating the grating pitch at the sample fabrication stage to achieve a specific SPR wavelength.

2.3 Surface Plasmon Polarization Conversion

The principal element of the devices used in this thesis is a crossed surface relief grating (CSRG) fabricated by the orthogonal superposition of two constant-pitch linear gratings written sequentially on an azobenzene thin film, as will be explained in the subsequent chapter. In this grating pattern, the grating vector $\boldsymbol{K}_1$ of the first linear grating is orthogonal to the grating vector $\boldsymbol{K}_2$ of the second linear grating.

When linearly polarized light is incident on a crossed grating, the grating that has its vector aligned with the light polarization will produce an SPR as explained in Paragraph 2.2.2. At a normal light incidence, a surface plasmon standing wave is generated [61]. This standing wave interacts with the second perpendicular grating in such a way that the energy of the SPR wave is transferred to the second grating following the reverse principle of the SPR excitation. The energy transfer happens due to the SPR electron plasma oscillations perpendicular to the grating surface. These oscillations are coupled to the second grating and the energy is re-emitted in the form of light. The phase-matching is ensured by the equality of the grating vectors magnitudes $K_1 = K_2$. Since the polarization of the light emitted by the second grating is parallel to its grating vector $\boldsymbol{K}_2$, the out-coupled light polarization is perpendicular to the polarization of the incident beam, i.e. polarization conversion happens [62].

The polarization conversion can be illustrated using a light transfer momentum model (k-space). In general case, the energy transfer condition for two orthogonal gratings depends on different combinations of the first polarizer orientation with respect to the gratings' vectors, the grating vectors relative magnitudes, and the angle of incidence θ of the irradiating light [62]. For the case when the light incidence angle is normal to the grating plane and the two grating pitches are equal (i.e. $K_1 = K_2$), the k-space diagram acquires the shape shown in Figure 2.7.

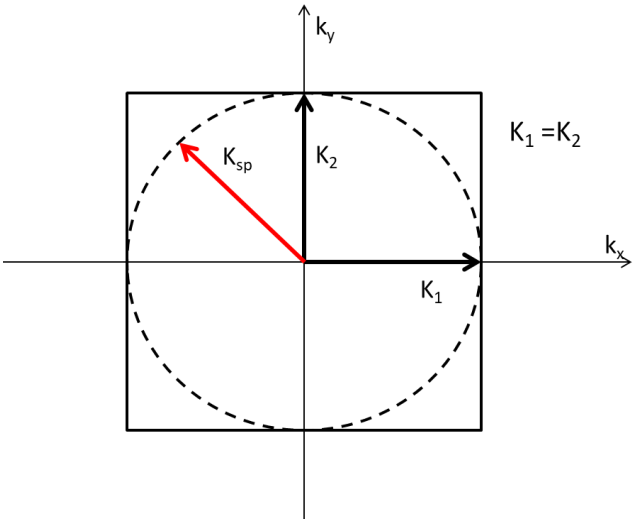

Figure 2.7: Momentum representation of SP polarization conversion in a CSRG irradiated with polarized light.

In this figure, the square represents the magnitude of the grating vectors K_1 and K_2, whereas the dashed circle represents the SPR standing wave.

The plasmonic energy exchange and the polarization conversion phenomenon described previously provide a remarkable possibility of using CSRGs for the elimination of all residual light from the light source and obtaining a narrowband signal of interest. This can be achieved by placing a CSRG between two orthogonal linear polarizers as shown in Figure 2.8.

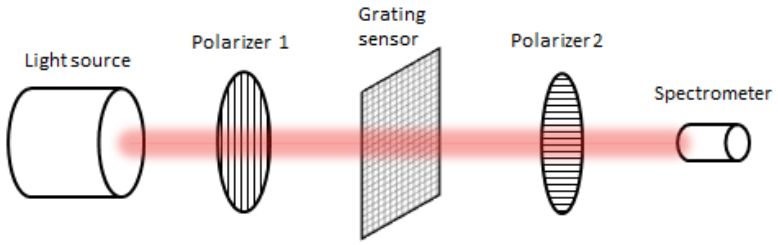

Figure 2.8: Transmission-based optical setup spectroscopy using crossed bigrating.

In this setup, both polarizers are perfectly aligned with the gratings. The first polarizer provides the beam polarization in parallel to one of the crossed gratings. The second polarizer passes only the out-coupled light with the polarization turned at 90° to the light incident on the CSRG, hence allowing the registration device (spectrometer, CCD diode, imaging camera, etc.) to capture only the converted SPR signal thus providing a very high signal-to-noise ratio.

3 Experimental Procedures

This chapter contains details about the sample preparation procedures, the spectral measurements, the surface grating profile measurements, the imaging techniques as well as the equipment used at all stages of the work. It includes information about the physical properties of the different samples and the inhomogeneous liquids used for imaging.

3.1 Substrate Preparation

3.1.1 Azobenzene Film Application

As discussed in Section 1.7, surface relief gratings can be fabricated using laser holography on an azobenzene thin film deposited onto a transparent substrate. The substrates were Corning soda-lime glass microscope slides with a 1 mm thickness. Two substrate sizes were used. Substrates with dimensions of 38 x 38 mm^2 were used at the beginning of the research for the grating parameters optimization. The size of the substrate allowed the inscription of several gratings (usually four) on a single piece. Furthermore, when the CSRG area was subsequently increased for the imaging experiments, only one grating was inscribed per substrate in order to avoid cross-contamination with the aqueous mixtures, the substrate's dimensions were changed to 25 x 38 mm^2. The substrates were cleaned with dish soap and warm water, wiped with lint-free Kimwipes, and dried in a Yamato oven at 100 °C for 20 minutes to evaporate any residual moisture.

A Disperse Red 1 molecular glass (gDR-1) compound was produced as described elsewhere [63] in the form of fine powder. It was dissolved in dichloromethane (CH_2Cl_2) at 3% weight/weight mix ratio. After shaking for one hour, the solution was filtered via a 45-µm filter. To obtain a thin film with the prepared solution, a spin coating technique was used. Prior to the gDR-1 solution deposition, the glass slides were cleaned with a blast of compressed air to ensure all residual dust was removed. Once clean, a substrate was placed in a Headway Research spin-coater chamber. Approximately 50 µL of the gDR-1 solution was deposited in the center of the substrate with a variable volume

single channel manual pipette. Then, the substrate was spun at 1100 rpm for 20 sec. After visual inspection of the obtained coating for surface imperfections, if not rejected, the sample was placed back in the oven for 20 min at 95 °C for residual solvent evaporation from the surface.

The film thickness was measured with a Sloan Dektak IID profilometer. The thickness of the films obtained under the described conditions varied from 250 to 300 nm. The substrates were then ready for grating inscription as described in the next section.

3.1.2 Crossed Surface Relief Grating Inscription

A CSRG on the azobenzene film was made using the experimental setup represented in Figure 3.1. A Coherent Verdi diode-pumped laser beam with a wavelength of 532 nm was passed through a spatial filter in order to reduce the Gaussian beam irradiation variation in the transverse plane and any aberration noise. The wavelength of 532 nm lies within the azobenzene *trans*-isomer absorption band hence, light at this wavelength induces the photoisomerization process necessary to generate SRGs. Then, the beam was collimated and passed through a quarter-wave plate generating circularly polarized light. The circular polarization was used because it was found to be the most efficient at writing gratings in azobenzene films. A variable iris was used to control the beam diameter so that the desirable grating area could be obtained on the substrate. At the grating parameters optimization stage, the iris was set to a diameter of approximately 9-10 mm. Later, to increase the grating area for the imaging experiments, the iris diameter was set to 14 mm.

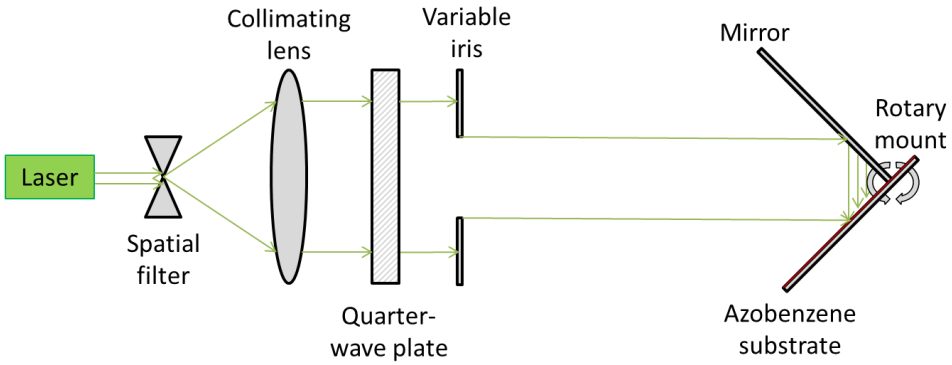

Figure 3.1: Optical setup for linear grating inscription.

In order to obtain a constant-pitch grating, a substrate was placed on a Lloyd mirror interferometer mounted on a rotating fixture with a vertical

rotation axis. In this configuration, the substrate was placed at 90° to a flat mirror with the mirror-substrate corner positioned at the center of the beam and the rotation axis. Hence, half of the laser beam was reflected from the mirror, while the other half was incident on the azobenzene film, thus creating an interference pattern, which would be imprinted on the film. The laser power was set to produce the irradiance of 428 mW/cm^2. The irradiance value was fixed for all gratings in this thesis, hence, the grating's depth would only depend on the exposure time.

The resulting grating pitch is determined by the laser beam incidence angle, which could be remotely controlled using a LabView software for adjusting the mirror angle. The grating pitch Λ depends on the mirror angle (θ) as defined by the following equation [46]:

$$\Lambda = \frac{\lambda}{2 \sin \theta}, \tag{3.1}$$

where λ is the laser beam wavelength (532 nm). The mirror angle calibration was checked prior to using the fixture for every substrate by setting in the LabView program the pitch value of 499 nm and verifying the reflected beam direction with respect to a known mirror orientation for this pitch.

Once the first grating was made, the sample was unfastened from the mirror, turned by 90° in the plane of the grating surface and placed back on the Lloyd mirror fixture. The substrate position alignment was such that a quarter-disc of the primary grating would overlap by a quarter-disc of the incident light yielding an orthogonally crossed surface relief grating (CSRG) covering a quarter-disc sector shaped area, as represented in Figure 3.2. Hereinafter, the convention accepted in this work designates the grating that was imprinted first during the fabrication as a primary grating. The grating imprinted atop of the primary grating is always referred to as a secondary grating.

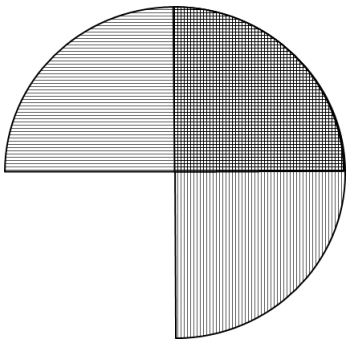

Figure 3.2: Crossed surface relief grating (CSRG).

All the setup parameters remained unchanged at that point except for the exposure time, which was the primary subject for optimization. Once the exposure time, and hence the grating depth, was optimized for obtaining maximum SPR signal strength, a CSRG pitch optimization procedure was carried out. This procedure resulted in obtaining the desired SPR signal peak position in the transmitted signal spectrum for the desired wavelength.

3.1.3 Silver Coating Application

As explained in Chapter 1 (Introduction), SPR excitation is possible on a metal-dielectric boundary. Therefore, the obtained CSRG on the azobenzene film had to be metalized. The final stage of the grating fabrication is a metal coating deposition. A layer of silver was applied using a Bal-Tec SCD-050 sputter coater. In earlier work [46], it was found that 60 nm silver thickness provides the highest SPR signal. The silver film thickness is measured using a Sloan Dektak IID profilometer.

3.2 Grating Depth and Pitch Measurements

An Atomic Force Microscope (AFM) (Bruker, Massachusetts, USA) was used to image the produced gratings during the CSRG optimization stage. Hereinafter, the AFM was used for the CSRG depth mapping in order to obtain the SPR contrast imaging brightness dependency on the CSRG depth.

The AFM allows obtaining a three-dimensional map of the CSRG surface, which can be stored and subsequently analyzed with the NanoScope Analysis 1.50 software program. The core technology of the AFM, PeakForce Tapping [64], uses a needle-tip probe to periodically tap the sample surface. The force from each tap is registered and the data on the height of the surface is registered along with the probe coordinates, thus building a 3D-image of the

scanned surface. An example of an AFM scan and a grating cross section is shown in Figure 3.3.

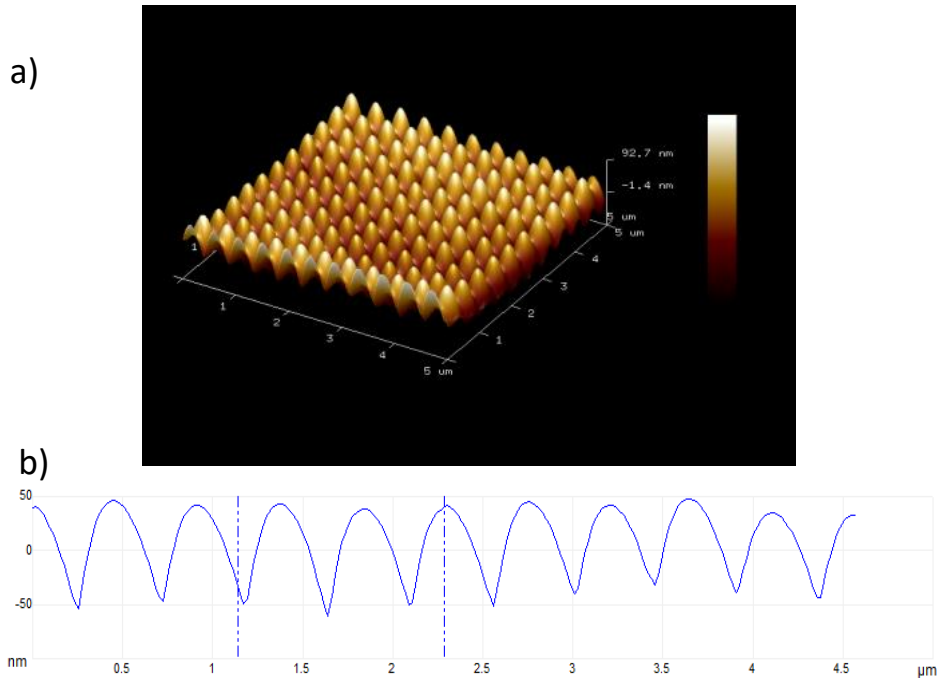

Figure 3.3: SRG AFM image: a) CSRG 3D surface rendering; b) gratings cross-section example.

Prior to beginning a scan, the sample was placed on the vacuum chuck with the primary grating grooves – the one which was inscribed first - oriented along the *y* coordinate axis. Hence, the primary grating vector would be aligned along the *x*-axis, which was parallel to the scan direction. Several spots evenly distributed over the CSRG quarter-disc sector were scanned. The AFM Nanodrive software allows the computerized positioning of the test sample in order to scan various areas with respect to a set origin with a precision of 0.5 nm. Each scan area was set at 5x5 μm^2 with a scan rate of 1 Hz per line. The grating pitch and depth were measured as an average from the obtained 3D surface image over the maximum number of peaks and troughs on each scanned area.

3.3 Spectrum Measurement

For this work, the optical characterization of the acquired SPR signals was done by measuring the transmission spectrum with an Edmund Optics CCD fiber

spectrometer using a set of optical elements aligned on an optical rail as illustrated in Figure 3.4. In the transmitted beam, the SPR energy transfer is observed as a peak in the spectrum at the SPR excitation wavelength [62, 65].

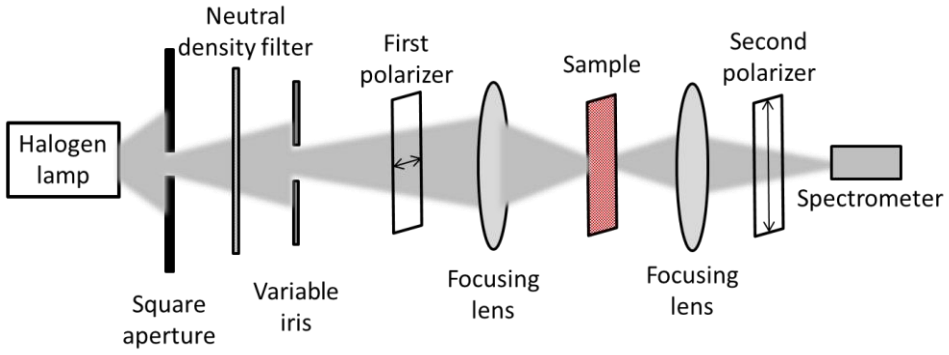

Figure 3.4: Transmission spectrum measurement setup scheme.

The white light was generated by a 12 V, 50 W, Oriel Corp. halogen lamp. The light was passed through a square aperture and then a variable neutral density filter in order to avoid a signal saturation in the spectrometer, while keeping the acquired signal at a maximum. Then, the light beam passed through a variable iris followed by a horizontally aligned linear polarizer. Then, using a convex focalizing lens with the focal length of 20 cm, the light was focused on the metal CSRG surface forming a spot of approximately 1 mm in diameter at normal incidence. In order to recollect all the light, which passed through the sample, it was then focused with a second lens, identical to the first one. The focused light was then passed through the second linear polarizer with its axis perpendicular to the first polarizer's direction in order to eliminate all residual non-SPR light from the halogen lamp, thus ensuring that only the light resulting from the SPR polarization conversion is captured by the spectrometer. The spectrometer allows detection of wavelengths ranging from about 400 nm to 900 nm. The data collection was done at an integration time of 100 ms.

The above-described light spectrum measurement technique was used for the grating depth and pitch optimization of both perpendicular CSRG gratings. The final goal of the CSRG pitch optimization was to find a pitch value, which ensures that the SPR signal peak wavelength was at the desired position in the obtained spectrum when water was placed over the CSRG and for a wavelength of 632.8 nm.

To create a metal-solution boundary, an opening was cut in a 2 mm thick slab of PDMS prepared beforehand. The opening dimensions allowed to cover the whole quarter-disk CSRG surface. The PDMS adhesion to silver is enough to attach the obtained carved shape to the sample surface with no additional glue substance. The carved PDMS slab was placed atop of the CSRG area and filled in with the glycerol solution and covered with a microscope cover glass to avoid the liquid leakage. At the same time, the cover glass flattened the surface of the liquid in order to eliminate lensing effects as illustrated in Figure 3.5.

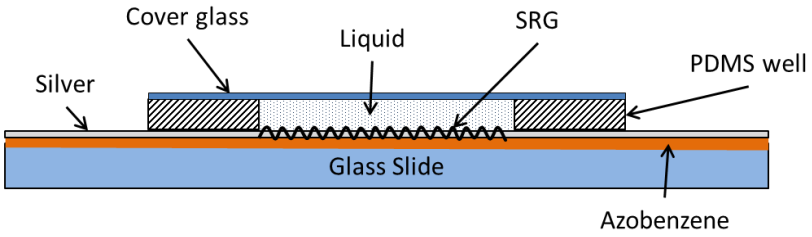

Figure 3.5: Cross-section of a tested sample.

This setup was used for the SPR wavelength characterization with respect to the dielectric medium refractive index change, as described in the next section.

3.4 Sensing Via Refractive Index Change

As discussed in Section 1.5, SPR sensing is based on the transmitted (or depending on the sensor type, reflected) light intensity change due to a variation in the dielectric medium refractive index (RI) on the metal-dielectric interface. Therefore, the SPR polarization conversion signal strength, which indirectly corresponds to the SRG grating quality, can be estimated by observing the SPR signal peak shift in response to the dielectric RI change. Thus, an SPR wavelength shift as a function of the RI can be used as a tool for characterizing the bulk sensitivity of this SPR device. For this purpose, aqueous glycerol solutions of different concentrations (from 0 to 25 % with an increment of 5%, weight/weight) were prepared using a Fisherbrand Isotemp Stirring Hotplate (SP88854200). For each solution, the spectrum of the light transmitted through two crossed polarizers and a CSRG was registered with the setup described in the previous paragraph.

3.5 Imaging Via Refractive Index Change

For this part of the work, a camera was used to image the RI change of the tested liquid media. For this purpose, aqueous sucrose solutions of different concentrations (0, 5, 10, and 15%) were prepared.

The characterization was carried out by comparing the brightness of the overall image obtained by the camera with the transmitted SPR light intensity captured by a photodiode and registered with a lock-in amplifier. These data were also compared with the signal level at a wavelength of 632 mm measured with the spectrum measurement procedure as explained in Section 3.3.

For the transmitted signal intensity measurement setup using a lock-in amplifier, the optical elements were aligned on an optical rail as illustrated in Figure 3.6a. The image intensity measurement setup with the camera is represented in Figure 3.6b.

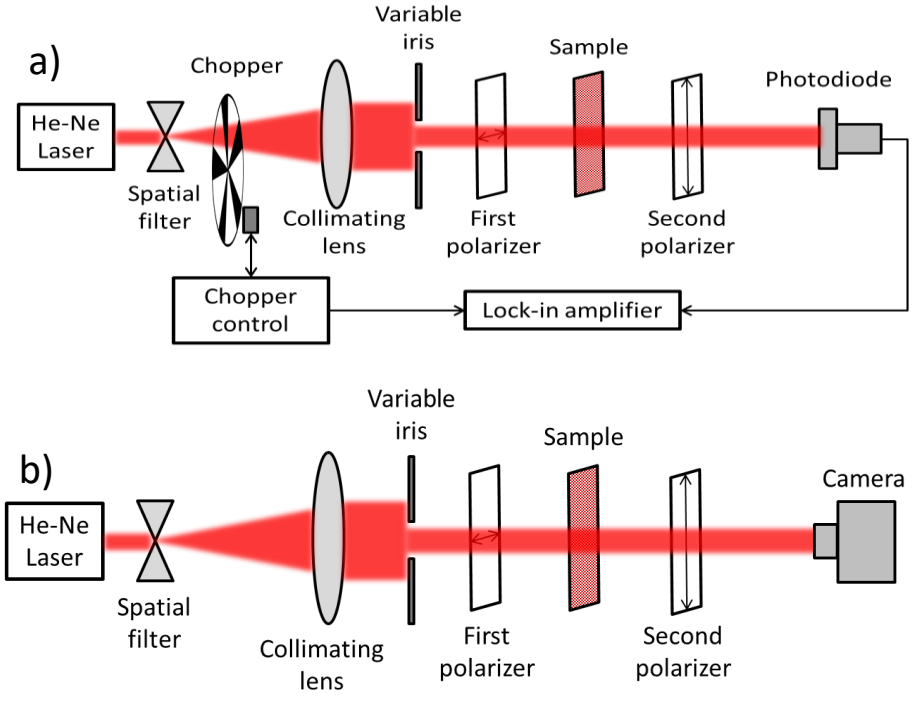

Figure 3.6: a) Transmitted signal intensity measurement with a lock-in amplifier; b) Transmitted signal intensity measurement with a CCD camera.

In the lock-in amplifier scheme, coherent light at a wavelength of 632.8 nm was generated with a He-Ne laser (JSD Uniphase, model # 1125, 2

mW). The light was passed through a 50-µm spatial filter to enable collimating and expanding the laser beam. A Stanford Research Systems lock-in amplifier was included in this setup as shown in Figure 3.6a in order to ensure very accurate capturing of intensity changes of the SPR light transmitted by the sample. The light coming from the spatial filter was passed through a rotating mechanical chopper connected to the amplifier through the chopper control unit. Then it was collimated and passed through a variable iris, creating a beam approximately 2.5 mm in diameter. A beam of this diameter formed a spot on the sample's surface covering about one-fourth of the CSRG area as illustrated in Figure 3.7. After the iris, the light beam passed through a vertically aligned polarizer and then through the sample, which was placed on a vertically and horizontally adjustable holder. The CSRG's primary grating grooves were oriented horizontally in order to provide consistency with the samples' orientation during the spectrum measurement procedure. Then, the light transmitted by the sample was passed through a second linear polarizer with its axis perpendicular to the first polarizer's direction, thus ensuring that only the light resulting from the SPR excitation is registered by the photodiode. The value of the current generated by the photodiode was then displayed on the lock-in amplifier display and recorded. The sample and the photodiode's vertical/horizontal position were adjusted in order to obtain maximum signal strength.

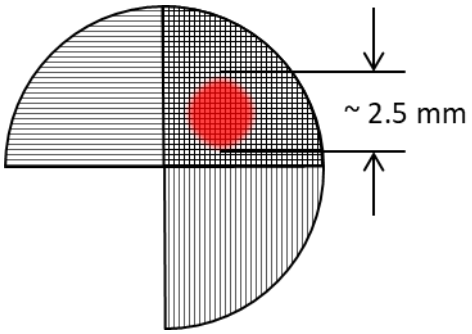

Figure 3.7: Sample illumination for transmitted signal intensity measurement.

After the transmitted signal intensity had been measured with the photodiode, the chopper was removed from the light path and the photodiode was replaced with a high-dynamic-range monochromatic CCD camera with 762x576 pixel matrix (Edmund Optics EO-04138M MONO HDR), which was installed on a separately adjustable fixture. The image from the camera was

displayed on a computer monitor allowing visual control of the camera position with respect to the light spot. The camera position was adjusted so that the light spot was centered on the camera's CCD sensor. A raw image with no software filtering was recorded in the BMP format with 8-bit, 256-level greyscale. Subsequently, the obtained BMP image was converted to a data format allowing the obtaining of an average value of the level of gray of the whole image matrix.

After the intensity and image brightness data were collected, the sample was placed in the spectrum measurement setup and the SPR spectrum data were recorded as described in Section 3.3. For each tested sample, the signal strength was registered at a wavelength of 632.8 nm only.

The described three-stage procedure, which includes the transmitted signal intensity measurement with a photodiode, the transmitted signal intensity measurement with a camera, and the SPR spectrum measurement, were repeated for each selected sample with different sucrose concentration (0, 5, 10, and 15%). The data sets obtained from each measurement procedure were normalized to their maximum and compared for each sample. An example of a resulting plot combining the three procedures' results, as functions of the bulk RI for one sample, is shown in Figure 3.8.

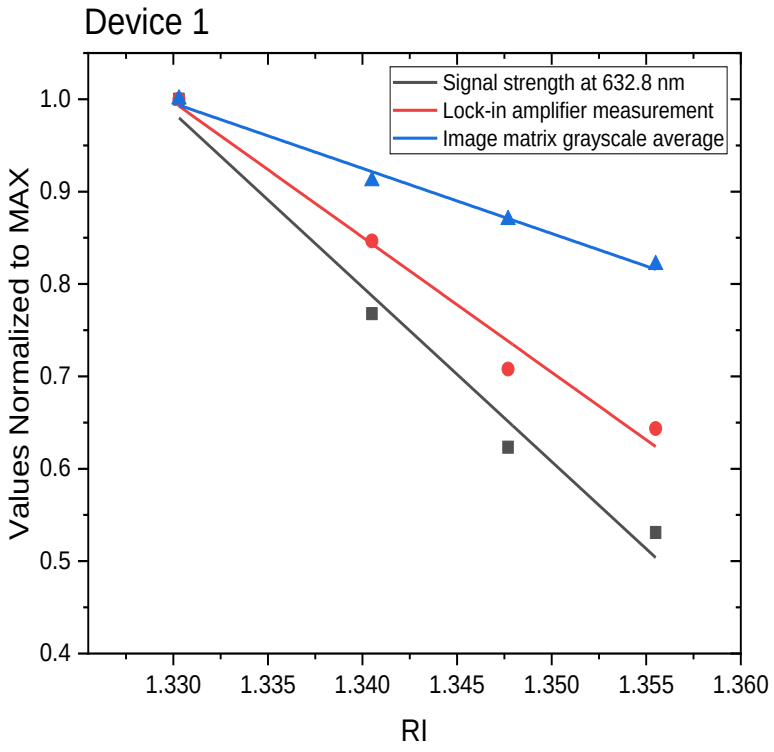

Figure 3.8: Signal strength at a wavelength of 632.8 nm, signal intensity measured with a lock-in amplifier, and images brightness measured for a sample as functions of the bulk RI and compared on a single plot.

Thus, the correlation between the SPR spectrum change, the SPR transmitted light intensity change, and the image brightness variation with respect to the bulk RI changes could be observed.

3.6 Microscopy Imaging of Inhomogeneous Mixtures

Two different setups were arranged to obtain images of inhomogeneous mixtures. In both setups, the samples were irradiated with light at 632.8 nm wavelength. The key difference between the microscopy imaging setups was that in one of them a coherent light beam from a laser was used, while for the second setup, an incoherent white light beam was filtered with a 632.8 *nm* narrow band filter.

For this work, five types of inhomogeneous aqueous mixtures were made, using: silicon oil (CAS# S159-500), white mineral oil (CAS# 8012-15-1), corn starch (regular commercial grade), silica gel particles of 63-200 μm size (CAS# 112926-00-8), and silica gel particles of 2-25 μm size (CAS# 112926-00-8). Different mixture components were used in order to obtain a variety of mixtures in terms of components' RIs, particle's sizes, their interaction with the CSRG's surface, and their behaviour during mixture separation/sedimentation process. All mixtures were prepared with deionized water. Due to the quick separation of the oils in water and the short sedimentation time of the silica gel and the starch particles (within a minute), it was found that the exact substance/water ratio of these mixtures is of minimal importance for this work and can vary widely. A more important factor was the time frame within which the images were taken after a sample installation on the test holder. For the oils, the mixtures with the concentration from 1 to 5% (w/w) were tested with equal imaging outcome. For the silica gel and the starch, the concentration was approximately 1-3%.

3.6.1 Microscopy Imaging of Inhomogeneous Mixtures Irradiated with Coherent Light

For the microscopy imaging of inhomogeneous mixtures irradiated with coherent light, the optical setup is similar to the one used for the transmitted signal intensity measurement setup with the CCD camera. The images were obtained with a focusing convex lens placed between the second polarizer and the camera, as illustrated in Figure 3.9. This was done so that the light coming from each micron-size area of the SRG would be expanded on several elements of the camera sensor (the sensor pixel size is 10 μm) in order to obtain better images.

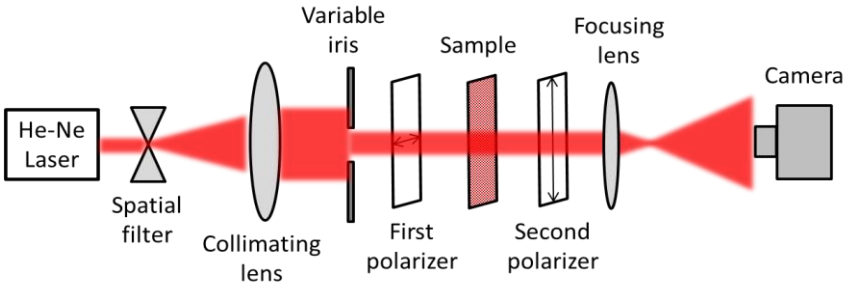

Figure 3.9: Imaging of inhomogeneous mixtures with coherent light irradiation.

To choose a better grating area for imaging in terms of visual brightness of the image on the computer monitor, the sample was first prepared with pure deionized water and placed vertically on the holder as illustrated in Figure 3.10.

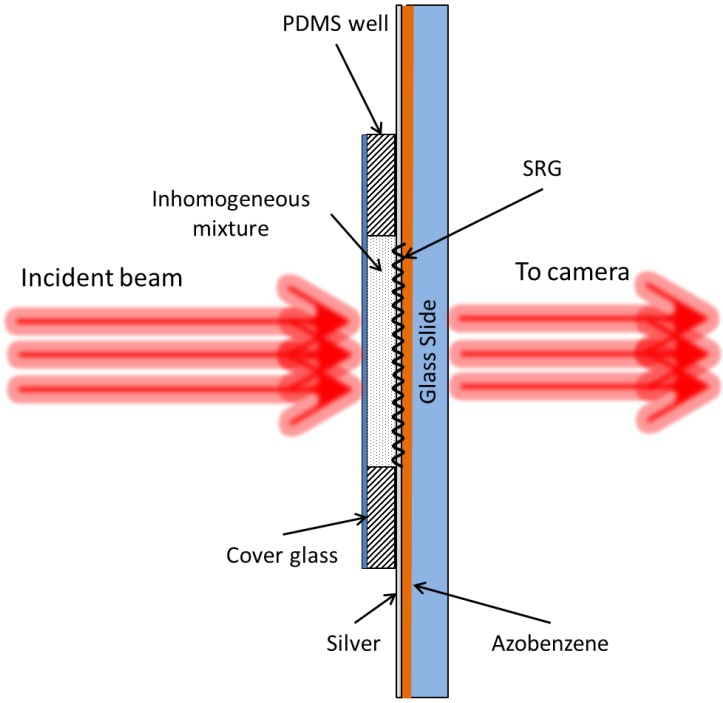

Figure 3.10: Sample setup for imaging.

Adjusting the variable iris, the irradiated area diameter on the CSRG was set at approximately 2.5-3 *mm*. With the camera and the sample holder position adjustment, a zone of interest was chosen with the help of the image displayed on the computer monitor by the camera software. Then, the sample was removed from the fixture and the water in the sample was replaced by an inhomogeneous mixture. Before being placed on the CSRG, the mixture was thoroughly shaken by hand in a 10-ml vial. After the mixture replacement, the sample was placed back on the fixture. The images were registered in a timeframe within the mixture separation/sedimentation period in order to capture not only the mixture particles held on the grating surface but also the particles in motion. The format of the registered images was 8-bit BMP 256-level grayscale for still images. Also, to capture the quick picture changes due to the mixture separation/sedimentation, videos were taken in the AVI format. Furthermore, the obtained AVI-files were converted into sequences of BMP still

images using a publicly available online converter www.filezigzag.com with a conversion rate of 10 images per second.

3.6.2 Microscopy Imaging of Inhomogeneous Mixtures Irradiated with Incoherent Light

The optical test setup for the imaging of inhomogeneous mixtures irradiated with incoherent light was similar to the one used for the spectrum measurement of the SPR signals as described in Section 3.3. The difference was that the fiber spectrometer was replaced with the CCD camera and a narrowband 632.8 *nm* filter was added as shown in Figure 3.11.

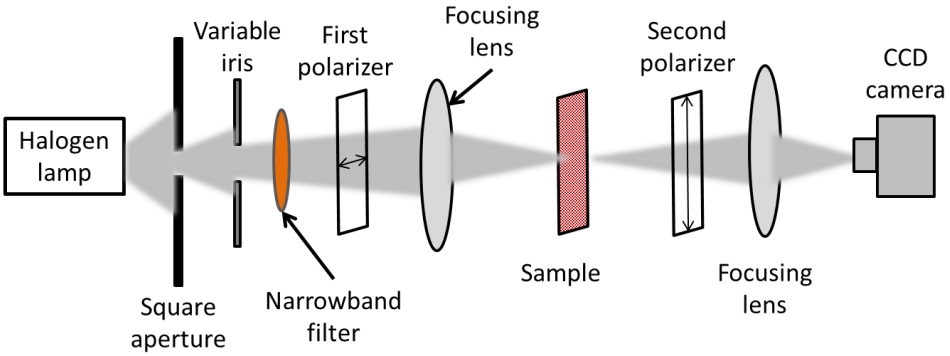

Figure 3.11: Inhomogeneous mixture imaging setup using incoherent light.

The sample handling and the imaging technique were analogous to the one for the coherent light imaging described in the previous paragraph.

Also, the average image intensity was recorded upon varying the water RI in this setup. The image recording was repeated at the same area of the CSRG for aqueous glycerol solutions of different concentrations (0, 5, 10, 15, 20, and 25%) used as dielectric media atop of the grating. The glycerol concentration variation allowed simulating bulk RI change which was measured with an Abbe Refractometer. All images were registered with no software filtering and at the same software brightness settings. The variation of the average level of gray calculated from the obtained BMP image data files was then compared with the visual brightness variation of the registered images.

The setup illustrated in Figure 3.11 was also used to observe a correlation between the grating depth distribution and the brightness of the images across the CSRG. For these purposes, images were taken in several places evenly distributed over the CSRG for a sample with pure deionized water.

Furthermore, they were compared with the depth distribution map plotted with the use of the data obtained from the AFM depth measurements as described in Section 3.2.

In addition, this optical setup was used for the visual demonstration of the SPR propagation length. For this, 62-68 μm wide scratches were made on the CSRG area by a sharp metal pin. The scratches width was measured with a Sloan Dektak IID profilometer. Also, light-blocking objects were made of black adhesive tape in the form of rectangles and triangles of overall dimensions of 1.5 x 1.5 mm^2. They were placed at the proximity to the scratches allowing imaging the scratches and the light-blocking objects on the same picture and comparison of the SPR propagation across the edges of the artifacts.

4 Results and Discussion

The ultimate goal of this thesis was to record microscopic 2-dimensional images of inhomogeneous mixtures based on the SPR intensity variation due to the mixtures' RI spatial distribution along the metal-mixture interface utilizing a high-dynamic range camera. The images were obtained using a narrowband CSRG with grating pitches optimized in a way that the resulting SPR signal peak of the transmitted light was maximized near a wavelength of 632.8 nm. The maximum SPR wavelength shift was found to be on the left-hand slope of the SPR spectrum, as illustrated in Figure 4.1. This point corresponds to the highest slope of the plot in Figure 4.1.

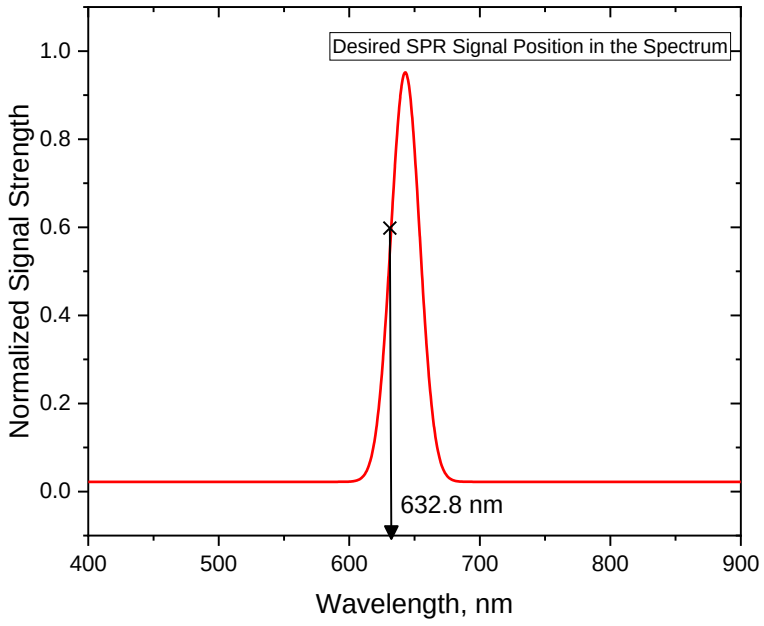

Figure 4.1: Desired resulting SPR peak position in the spectrum.

This chosen wavelength position in the spectrum above ensures that a large change in the signal strength at a wavelength of 632.8 nm occurs due to a change in the tested liquid RI. Thus, a monochromatic image of the spatial RI variations would be created in the transmitted signal and captured with the camera.

The fabrication of a CSRG providing this desired effect included the grating parameters optimization in order to obtain the strongest signal possible at the desired position in the spectrum. These optimized parameters include the gratings' depth and the gratings' pitches, both of which could be controlled during the CSRG laser inscription process described in Paragraph 3.1.2.

4.1 SRG Optimization

4.1.1 Grating Depth Optimization

The CSRG depth was the first parameter to be optimized in order to obtain two gratings with depth values close to each other as much as possible. Since the superposition of two gratings requires an inscription of one of the gratings on top of the other, the inscription times for both gratings must be different because the secondary grating is inscribed in an already modified film surface and the secondary peaks and troughs formation conditions are different. Different inscription times allow the equalization of the depths of both gratings as much as possible in order to provide maximum energy transfer between the gratings as explained, in Section 2.3. Since several CSRG optimization processes had been done previously for different purposes and the results were published in the literature [42, 46, 66], there was no necessity to carry out a full-scale optimization with wide inscription time variations and the results obtained in the past in our research group could be used as a starting point. These tests were done with the purpose of ensuring that the grating inscription setup allows using the inscription time values similar to the previously obtained results. The values reported by Bdour et al. of 120 secs inscription time for the primary grating and 60 secs for the secondary one at an irradiance of 428 mW/cm^2 were used at the beginning of the optimization procedure in this work [66]. The gratings' depth optimization was made in air to facilitate the sample handling and the SPR spectrum measurements. The grating pitch was chosen to be 615 nm, which in theory, using Equation 2.65 gives a resulting peak at ≈632.5 nm for the SPR wavelength. This theoretical value was chosen because it is located in a bandwidth where the azobenzene film is almost transparent, thus allowing

obtaining better SPR signal in transmission. At the same time, the chosen grating pitch would serve as a starting point in the optimization procedure for samples with water as a dielectric.

First, the only parameter that was changed was the secondary grating inscription time with the first grating's inscription time kept at *120* secs. Ten gratings with the inscription time from 30 to 90 secs were produced. Only five samples with the inscription time close to 60 secs produced a significant SPR peak. Their spectra were normalized to the level of the signal passed through a sample area with no grating, as illustrated in Figure 4.2.

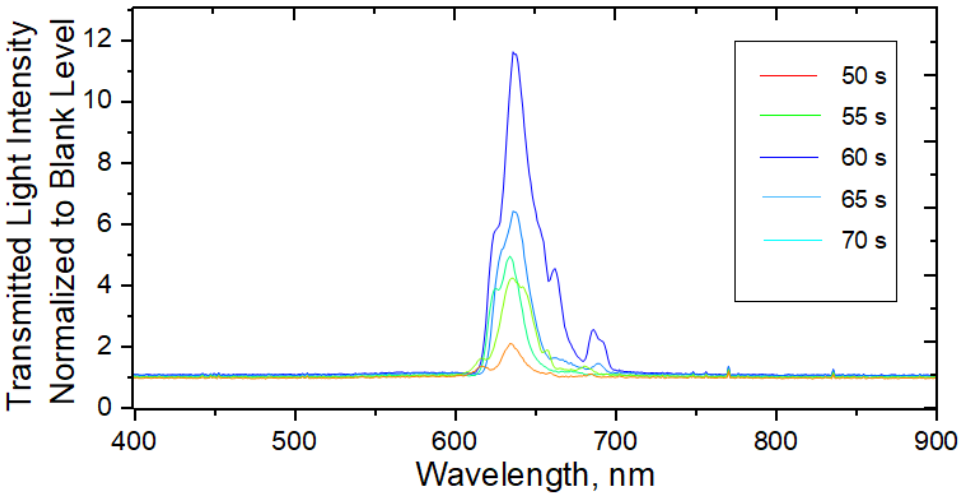

Figure 4.2: Transmission spectra of CSRGs with 615 nm grating pitch for different secondary grating inscription times; primary grating inscription time is 120 secs.

As seen in Figure 4.2, the best result was shown by the sample with 60 secs inscription time for the secondary grating, which is consistent with the results obtained in earlier work [66].

To ensure the completeness of this part of the CSRG's parameters optimization, the primary grating's inscription time for several samples was varied up to 300 secs, while maintaining the secondary grating inscription time at 60 secs. Figure 4.3 represents the spectra of the transmitted signals for the samples fabricated with the primary grating inscription time of 120, 150, 200, and 300 secs. As seen in Figure 4.3, the signal obtained with the sample made with an inscription time of 120 secs for the primary grating remains the strongest of all. Furthermore, the samples with longer inscription times

generated peak-splitted signals due to the SPR band gap resulting from a too-deep primary grating.

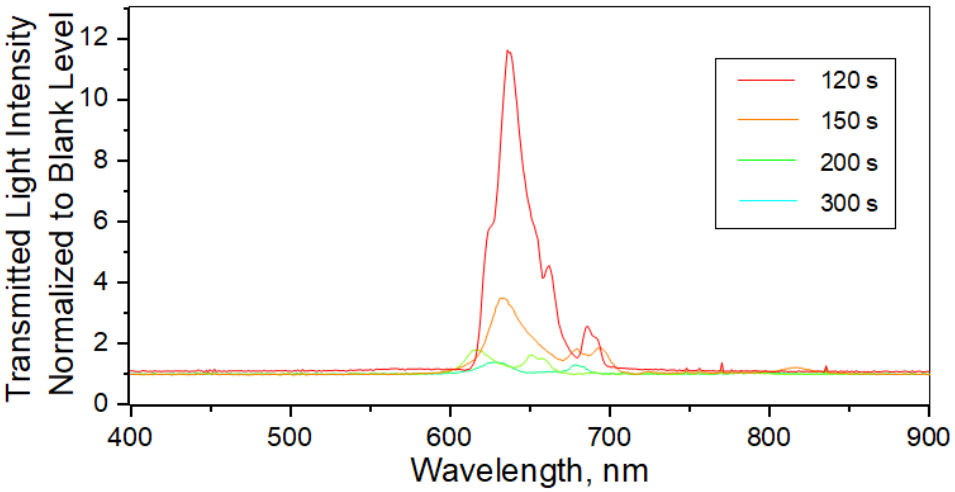

Figure 4.3: 615 nm pitch CSRG transmission spectra for different first grating inscription times; secondary grating inscription time is 60 secs.

Hence, it was reconfirmed that the inscription time of 120 secs for the primary grating and 60 secs for the secondary one would provide CSRGs deep enough to generate the highest possible SPR energy conversion in transmission. At the same time, this inscription time ratio avoids the SPR band gaps generated in the spectrum as explained elsewhere [67]. These band gaps would lessen the SPR signal slope, and thus the sensitivity of the test device.

4.1.2 Surface Gratings Pitch Optimization

Once the optimal gratings inscription times were determined, both gratings' pitch had to be adjusted so that when pure water is placed on top of the grating, the SPR signal position in the resulting spectrum would be maximized at a similar wavelength of 632.8 nm as explained earlier in this section and illustrated in Figure 4.1. In this work, both pitches of the pair of orthogonal gratings were kept identical in order to fulfill the polarization conversion condition for normal incident light as explained in Section 2.3 "Surface Plasmon Polarization Conversion". Equation 2.65 derived in Paragraph 2.2.2 allows finding the required grating pitch for a specific SPR wavelength, dielectric's RI, and real part of the metal permittivity. As seen in Figure 4.1, to get the

wavelength value 632.8 nm in between the middle of the left slope and the peak, the SPR peak should be approximately at 645 nm. Using known values of the permittivities for water [68] and silver [69], the grating pitch value was computed to be 460 nm in order to obtain the SPR peak at 645 nm. This pitch value was a starting point for the pitch optimization procedure. As expected, the obtained SPR peak wavelength was different from the theoretical value because Equation 2.65 had been derived for a flat metal-dielectric surface and the CSRG was considered as an approximation of a flat boundary. The experimental peak wavelength was obtained at 660 nm. In order to get a satisfactory pitch value providing an SPR at 645 nm, two other samples with pitches of 440 and 450 nm were made and tested. The best result was obtained with a sample of 450 nm pitch, as illustrated in Figure 4.4. This value will be used as the gratings' pitch for both orthogonal gratings in all further experiments in this thesis.

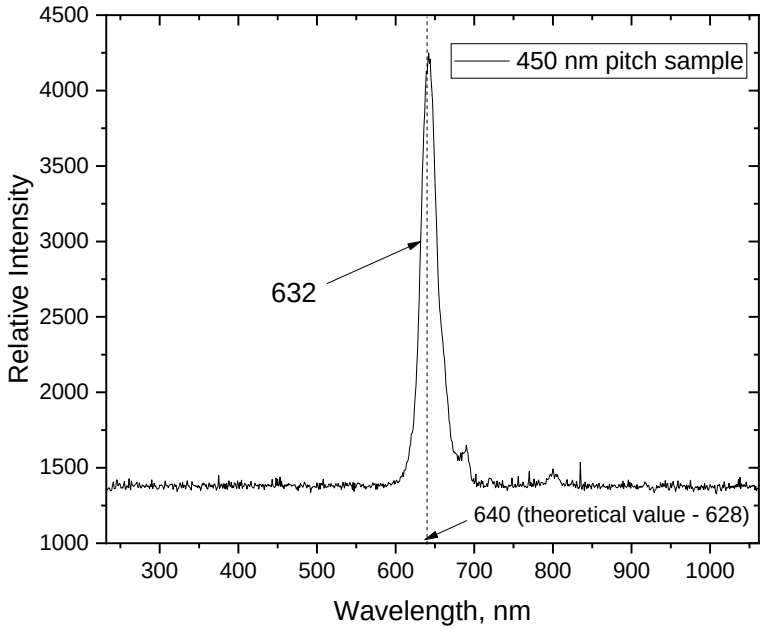

Figure 4.4: Raw transmission spectrum of a 450 nm - pitch CSRG covered with deionized water and irradiated with incoherent light at 632.8 nm as seen in the fiber spectrometer software BWSpec.

4.1.3 Sensitivity Tests

Once the CSRG depth and pitch optimizations were completed, a series of tests were carried out in order to obtain quantitative characteristics of the CSRG bulk sensitivity with respect to the dielectric medium RI change as well as to observe how the brightness of the 2-dimensional images captured by the camera correlated with the RI change.

4.1.3.1 Refractive Index Unit Measurements

First, to characterize the CSRG bulk sensitivity, five identical samples with the optimized parameters were fabricated and their spectra with water solutions of different RIs were measured. To simulate the RI change, several glycerol/water solutions of different concentrations were prepared, as explained in Section 3.4. Pure glycerol RI is 1.47399 [70]. This value is different from the water RI and glycerol is miscible in water, Therefore, bulk RI change simulation can be achieved by mixing glycerol and water in different proportions. The obtained solutions' RIs were measured with an Abbe Refractometer (type 2WAJ) and results are shown in Table 1 below.

Table 1: Glycerol solution refractive index.

Glycerol concentration, %	0	5	10	15	20	25
Refractive Index	1.333	1.338	1.344	1.349	1.354	1.359

Thus, for each one of the identical CSRG samples, the spectrum data was obtained for all the solutions listed in Table 1 and they were normalized to their maxima. Hence, the RI sensing experiment was repeated five times. An example of the redshift observed for a single CSRG device is illustrated in Figure 4.5. Since the redshift is small when compared to the spectrum bandwidth, the raw spectrum plot is zoomed around the 632.8 nm area in order to give a better visual representation of the spectrum shift. From Figure 4.5, it can be concluded that for this particular case, each concentration increment of 5%, increasing the RI by ~0.0055, caused approximately 0.84 nm redshift on average.

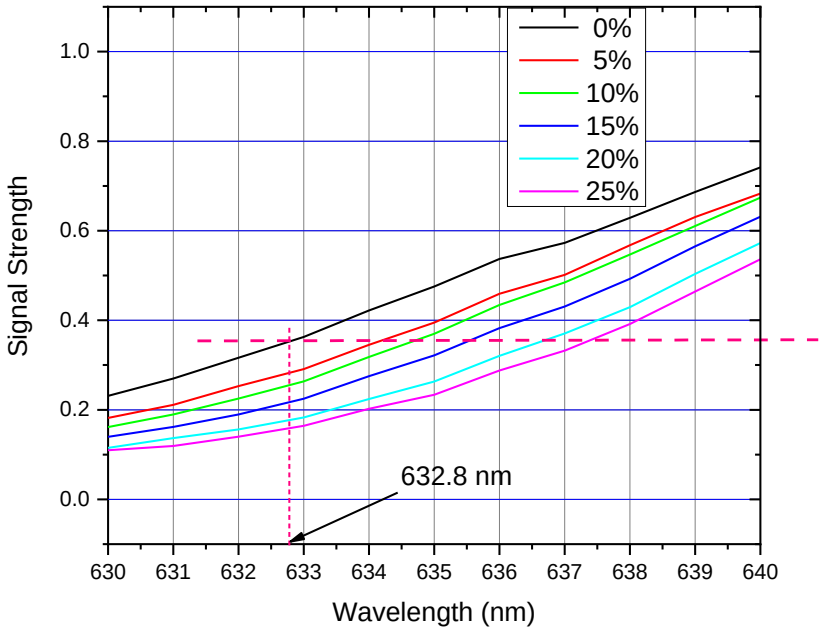

Figure 4.5: SPR spectrum redshift due to glycerol concentration change.

The SPR spectra for all five CSRG samples were processed and the redshift at the same normalized signal strength with respect to the wavelength of interest of 632.8 nm was recorded for each glycerol concentration. The sensitivity of the tested CSRG devices was calculated as a ratio of the SPR wavelength shift of the normalized spectra and the RI change. Figure 4.6 represents the sensitivity by a linear fit for all five devices. It shows that the highest obtained sensitivity for the tested samples was at the level of 223 nm/RIU, which is approximately three times lower than the bulk sensitivity reported in a previous work [66]. This difference is likely due to the fact that the higher sensitivity obtained in the earlier work [71] was because the SPR spectrum shift was measured at the SPR peak wavelength, while the SPR shift in this work was obtained at the maximum slope of the SPR spectrum to enable enhanced single wavelength microscopy rather than polychromatic spectroscopic measurements.

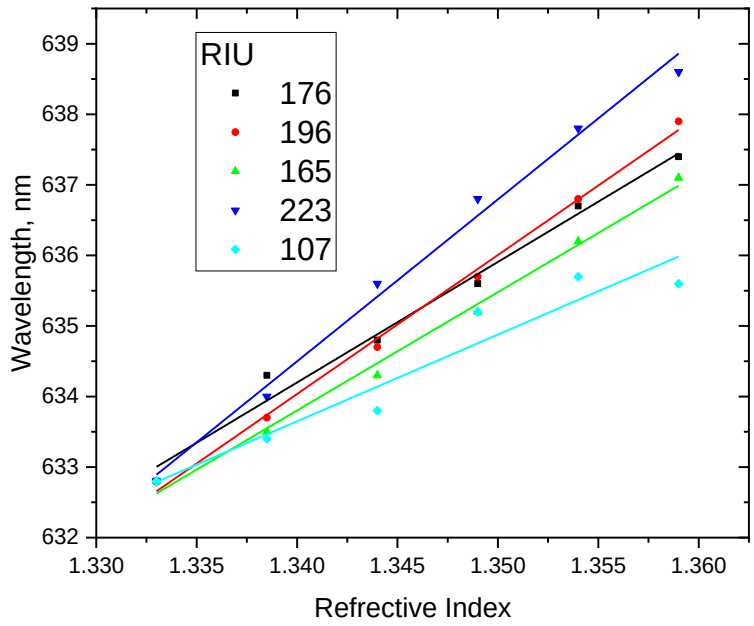

Figure 4.6: Sensitivity of the five devices.

4.1.3.2 Images' Brightness, Spectrometer, and Lock-In Amplifier Measurement Results Correlation

This part of the tests was carried out with the intent to observe how the overall brightness of the images captured by the camera correlates with the dielectric refractive index change. This is known as SPR imaging. Four identical devices were fabricated, as per the optimized parameters discussed earlier, for measurements with aqueous sucrose solutions of different concentrations (0, 5, 10, and 15%). These measurements were made using monochromatic light, with either the photodiode or the camera as described in Section 3.5. In addition to these measurements, spectra of the samples were also recorded using the fiber spectrometer when they were irradiated with white light. In the latter case, to obtain the bulk sensitivity at 632.8 nm, the SPR signal strength at that particular wavelength was selected. Thus, the transmitted light intensity for monochromatic coherent light obtained using either the photodiode or the camera, collected as average image brightness, and the transmitted white light

intensity at 632.8 nm were all used to calculate the SPR signal strength as a function of the RI. The results of all measurements were normalized to their maxima and combined into a single plot for each tested device as represented in Figure 4.7. The red linear fits correspond to the camera image brightness change, whereas the blue ones represent those from the photodiode measurements. The gray linear fit represents the SPR signal strength change at 632.8 nm wavelength as measured using the fiber spectrometer. The main goal of these tests was to ensure the camera's capability of capturing the light intensity change caused by the bulk RI changes would comply with the other methods of sensitivity detection. Thus, it could be confirmed that the SPR intensity variations caused by the dielectric RI change can be observed as the brightness variation mapped in the images obtained with the camera.

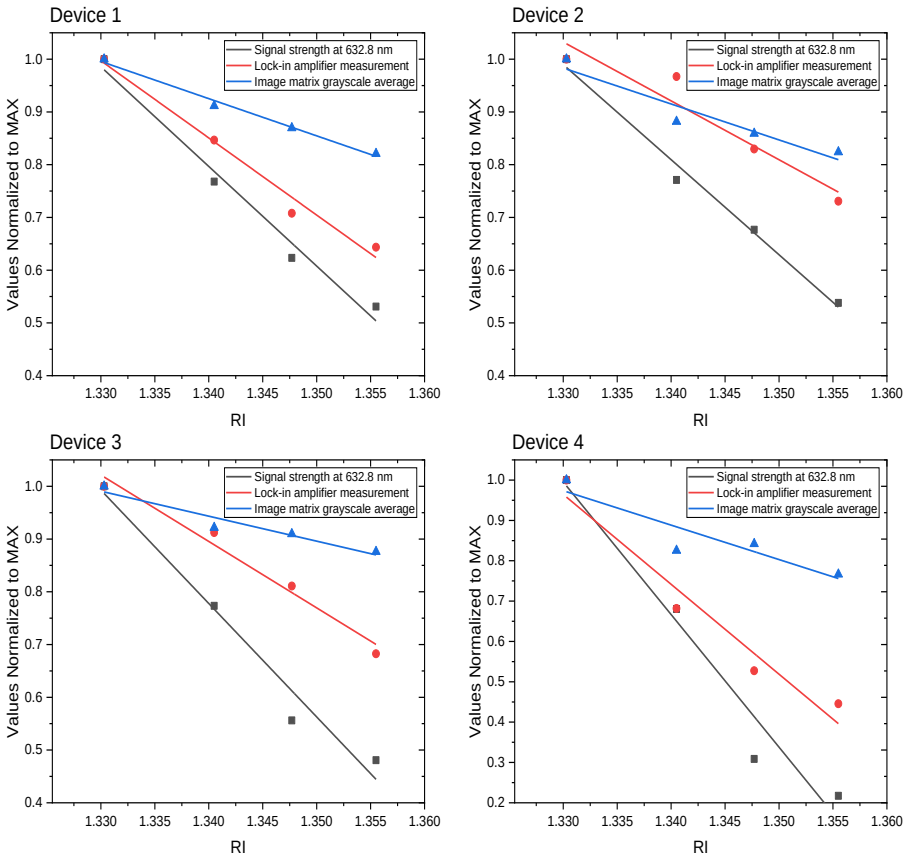

Figure 4.7: Correlation between spectrum measurements, signal intensity measured with a lock-in amplifier, and images brightness.

trend of decreasing values with increasing RI. The difference between the slopes of the red and blue lines can be explained by the fact that the camera hardware gain algorithm affects the resulting image. Another possible reason can be that the camera's software algorithm of the BMP file generation has its peculiarities in terms of the signal processing with respect to the level of dark. To ensure the consistency of the measurements, the settings of the level of dark in the camera software were kept unchanged. The slope difference between the grey lines and the red and the blue ones can be explained by the fact that the grey lines were obtained using a different optical setup, where incoherent white light was used. These slope differences were of minimal importance for this work. The

important outcome of these tests was that the camera was capable to accurately measure the dielectric medium RI changes.

4.2 Inhomogeneous Aqueous Mixture Microscopy using Coherent Light

In this part of the work, 2-dimensional images of the transmitted coherent light at a wavelength of 632.8 *nm* were recorded when different aqueous mixtures in the PDMS reservoir were placed on the CSRGs. First, microscopy images were taken using the camera as described in Paragraph 3.6.1, with the only difference being that the focusing lens shown in Figure 3.9 was initially removed. Thus, the transmitted light beam was passed through the second linear polarizer and directed straight to the camera. For a better understanding of the relative sizes of the objects in all images presented in this section, the camera sensor's physical characteristics are presented in Table 2.

Table 2: Camera's sensor dimentional specificaions.

Characteristic	Value
Pixels total quantity	0.4 MP
Matrix dimentions	768(H) x 576(V)
Active image area size	7.68 x 5.76 mm
Pixel size	10 x 10 µm(H x V)

4.2.1 Silicone Oil Mixture Imaging

For the first images, silicone oil mixtures of concentrations of 0, 2, 5, and 10% weight/weight were used on two devices. The resulting images are presented in Figure 4.7. Due to its low surface tension, silicone oil spreads easily over surfaces of various substances, therefore all surfaces inside the PDMS reservoir were partially covered with oil. No method was found to clean the samples without destroying the gratings. Therefore, any CSRG sample, once used with the silicone oil mixture, became unusable and had to be discarded. As seen in Figure 4.8, no valuable conclusion could be made at this stage of the experiments. Another factor impeding the obtaining of a quality image was the diffraction pattern of the laser beam. It is well seen in Figure 4.8 in the image of Device 1 with water (Silicone Oil 0%) in the form of the dark concentric circles.

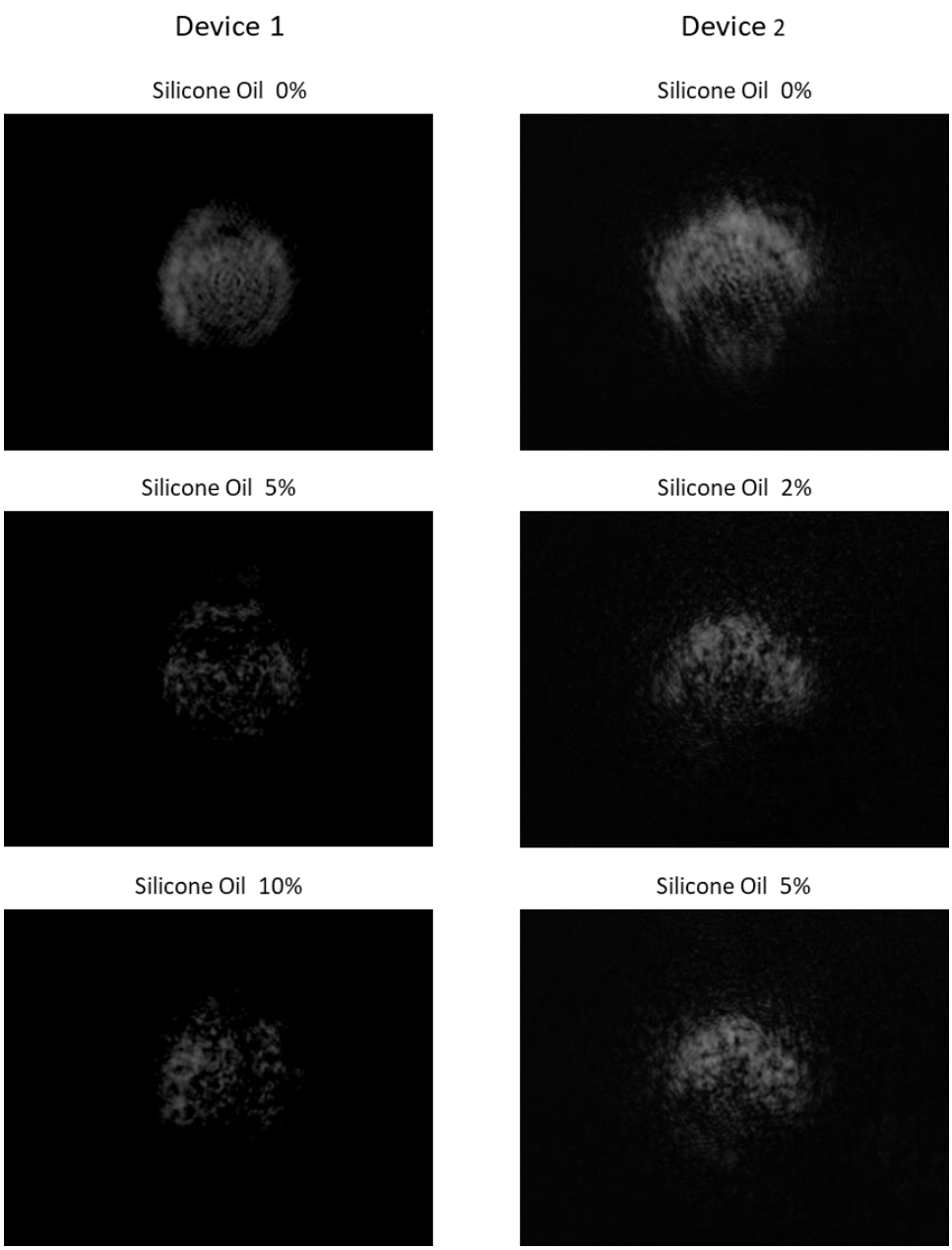

Figure 4.8: Silicon oil aqueous mixture images made with no optical magnification.

The presumptive cause of these circles was the spatial filter, which had a diameter of 50 µm. The attempts to use spatial filters of lesser diameters (10,

15, and 25 µm) led to a significant decrease of the light beam intensity resulting in the images' brightness decline when the raw images became too faint. This problem could be resolved by the image processing with image differencing software techniques or by using a more powerful light source and represents a subject for future work.

4.2.2 Corn Starch Mixture Imaging

The next experiment was carried out using the corn starch mixture. Corn starch is insoluble in water at ambient temperature and its particle size is within ~2-20 µm [72], which is comparable to the camera pixel size of 10 µm. Therefore, for this work, it was considered suitable for an inhomogeneous mixture preparation and imaging. As before, the first image had been made just with pure water in order to serve as a baseline for the subsequent images comparison. Then, right after the sample with the starch mixture was placed on the fixture, several images were taken with approximately 15 secs intervals. Figure 4.9 illustrates the images obtained during the starch sedimentation. This mixture caused significant light scattering, which can be seen as the light spot dimensions increase in comparison to the image of the pure water sample.

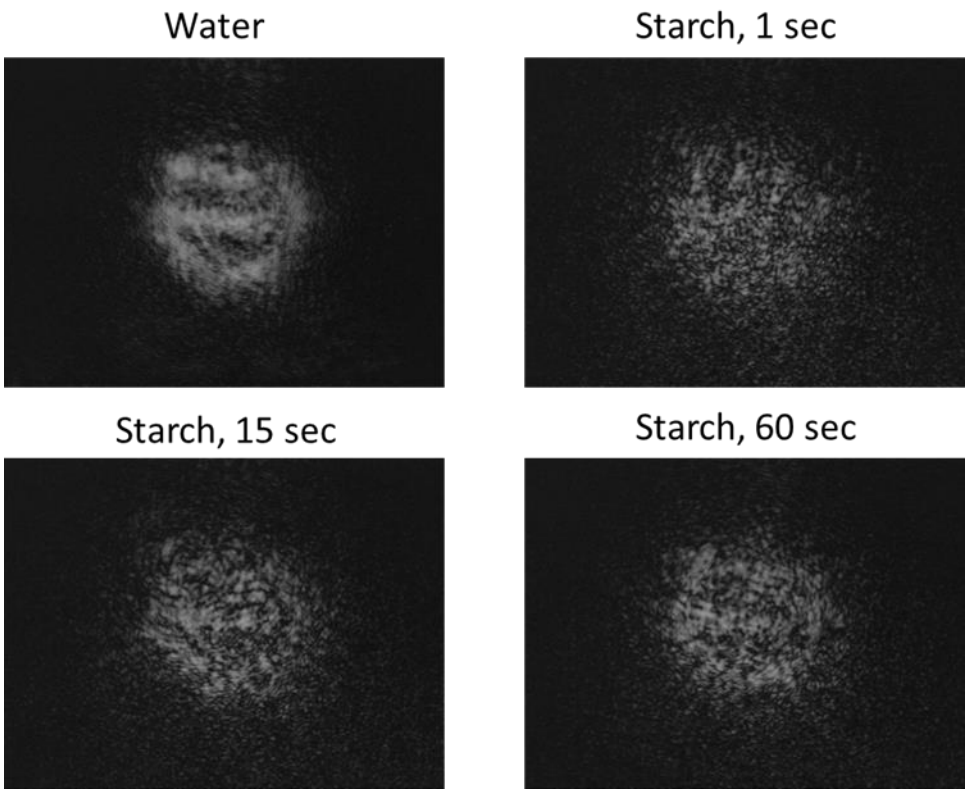

Figure 4.9: Corn starch aqueous mixture images were taken in different moments of the starch sedimentation.

It has to be taken into account that the resulting images in all cases (here and afterward in this work) were formed by the light passing through three different groups of the mixture particles in terms of their location in the PDMS well as shown in Figure 4.10: particles held on the grating's surface, particles precipitating/floating up in water, and particles held on the cover glass surface. Since the samples on the fixture were installed in a vertical position, the image pattern was changing in time due to the mixture separation. Recall that the SPR is confined to the metal-dielectric interface and the space of its existence in the dielectric is limited by 200-400 nm from the metal-dielectric boundary depending upon the metal/dielectric [56]. Therefore, the objects of interest for the SPR microscopy are the particles of Group #1, as illustrated in Figure 4.10. Only these particles cause the RI change affecting the SPR

propagation conditions on the metal-dielectric interface, thus creating the SPR image. All other particles in the reservoir represent light-blocking and light-scattering objects that can also be seen in the images. It is obvious that the shadowing caused by the light-scattering and light-blocking objects in the obtained images should be treated separately and eliminated from the resulting SPR images. Evidently, it is not possible in this work to distinguish between these two phenomena. The experimental setup and the sample preparation technique could perhaps be modified in future works in order to eliminate the shadowing caused by the light-attenuating objects.

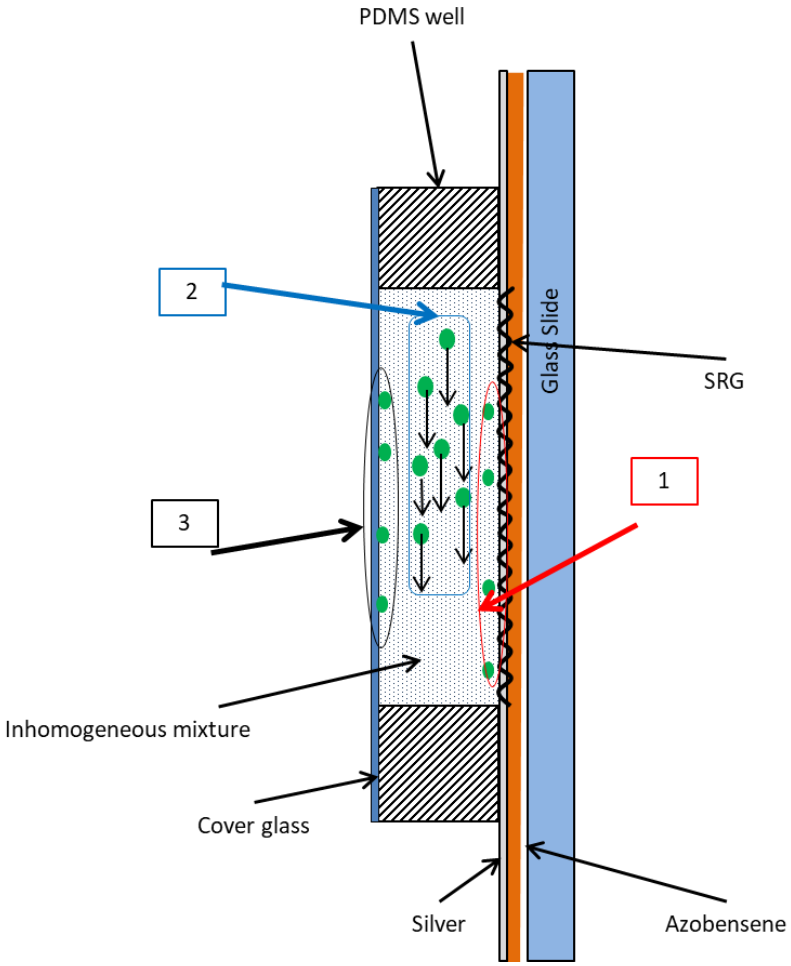

Figure 4.10: Particles' location in the reservoir: 1 - particles held on the grating's surface; 2 - particles precipitating/floating up in water; 3 - particles held to the cover glass surface.

4.2.3 Silica Gel Mixture Imaging

At the next stage of the tests using the coherent light setup and the camera, the samples were prepared with silica gel aqueous mixtures. First, the silica gel particles of 60-210 μm size were used to estimate the camera's capability to capture the difference with respect to the pure water sample image. Several video images were made and it was seen very clearly that the particles of this size produced circular light interference patterns moving across the image.

Figure 4.11 illustrates a difference image made with the help of Origin® software applying the simple mathematical subtraction of two images from the video. The bitmap image from the end of the video, when all particles had fallen down, was taken as the baseline. A BPM file containing the image at the moment when the particles were still in motion was chosen as a subtrahend. To enhance the resulting image the *imgGamma* function was applied and the brightness correction was made in Origin®.

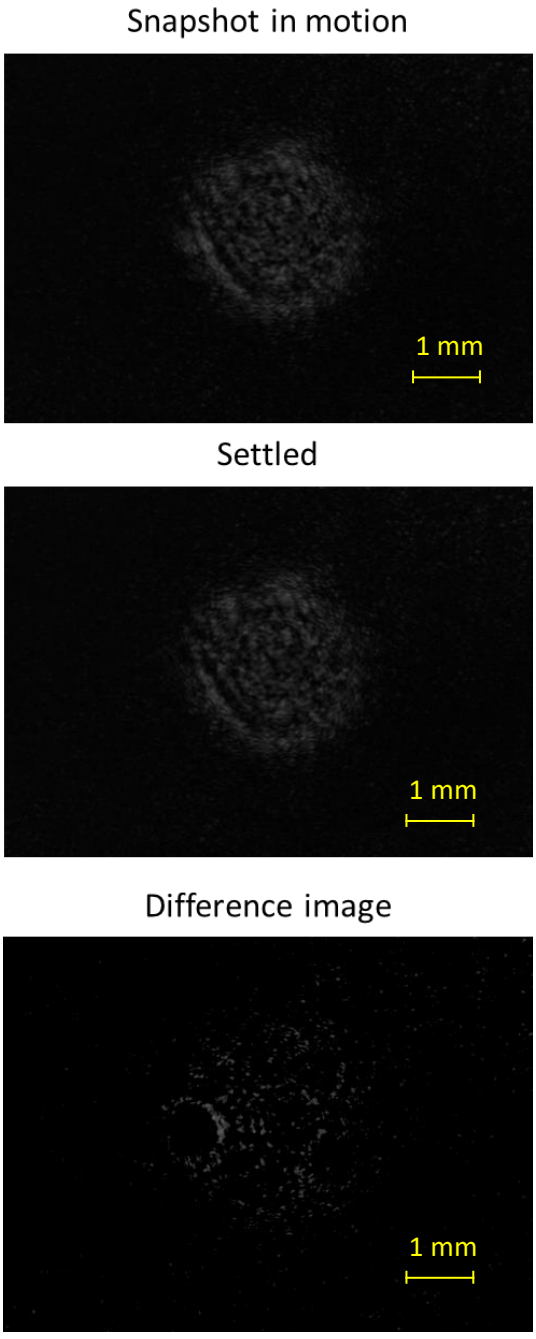

Figure 4.11: Difference image of silica gel 60-210 µm particles aqueous mixture in motion.

Then, smaller silica gel particles of 2-25 μm were used as a mixture component and multiple still images and videos were taken. This time, the images were taken with the transmitted light beam directed straight to the camera sensor as well as with the beam expanded by a lens in order to obtain more detailed images. In the former case, the particles were not distinguishable in the pictures because their size was close to the camera pixel size. In the magnified images, it was possible to observe patterns caused by the moving particles in water. It was also possible to see a difference between a baseline image taken after the particles' sedimentation was ended and an image arbitrarily chosen from the series of BMP files after the video conversion. The resulting difference image is represented in Figure 4.12.

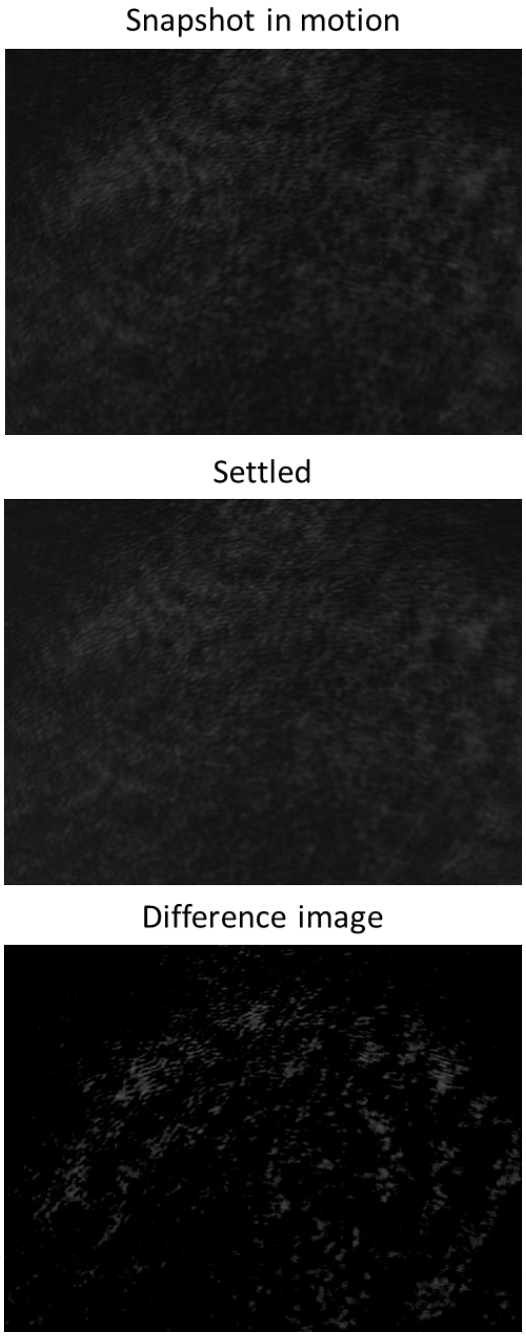

Figure 4.12: Difference image of silica gel 2-25 µm particles aqueous mixture in motion.

As seen in Figure 4.12, the granularity of the images does not allow a clear distinction to be made between the particles held on the CSRG and the cover glass surfaces and the baseline picture's irregularities. Supposedly, this granularity resulted from the coherent light interaction with the surface of the camera sensor, because this effect could still be seen when the sample and one of the polarizers were removed from the laser beam path. Also, the noise caused by the internal camera flicker also makes its input in the resulting image.

After all three mixture imaging experiments, it became clear that it would be probably impossible to obtain any meaningful imaging results with the chosen coherent light setup and the work passed to the next experimental stage using incoherent light.

4.3 Inhomogeneous Aqueous Mixture Microscopy Imaging using Incoherent Light

The very first steps in the experiments with incoherent light gave more valuable results in comparison to what was described in the previous section. All further experiments were performed according to the procedures explained in Paragraph 3.6.2 "Microscopy Imaging of Inhomogeneous Mixtures Irradiated with Incoherent Light". The quality of the images made with the incoherent light setup allowed carrying out more diverse experiments and to make some meaningful conclusions.

4.3.1 Images & Average Intensity vs Sugar Concentration

First, a test confirming the camera capability to capture the dielectric's bulk RI change was performed. It was similar to the image brightness measurements made with the coherent light and described in Paragraph 4.1.3.2. Aqueous sugar solutions of concentrations from 0 to 25% with an increment of 5% were used to simulate the bulk RI change. For each concentration, an image was registered, imported into Origin® and subsequently converted in a data matrix with 256-bit greyscale values generated by each camera sensor pixel. The brightness of the images was finally expressed in terms of the average value of each image data matrix as a function of RI, as shown in Figure 4.13.

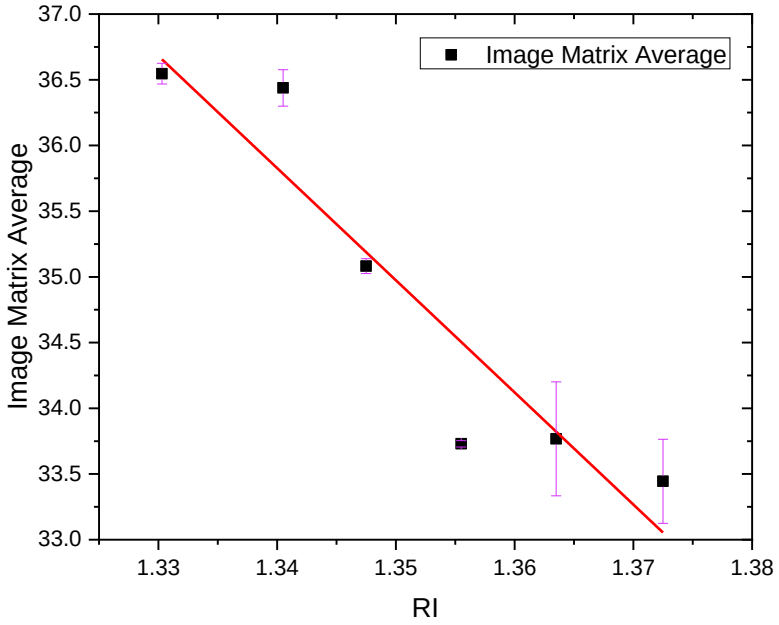

Figure 4.13: Image data matrix average value as a function of bulk RI.

For each RI, three images were taken and the error bars on the plot demonstrate the image matrix average value variation for each sample. The error bars were calculated as a standard deviation of data points from their sample mean. The large standard deviation variations of the image matrix average values for higher RI can be explained by the fact that due to the large redshift of the resulting SPR signal the wavelength of 632.8 nm does not correspond to the highest slope of the spectrum and the signal strength change is smaller and becomes comparable to the noise level. As seen in Figure 4.13, the image matrix average variation happens within a very tight range, when the delta between the marginal values is about only 4 level units of the greyscale, which is a very small value compared to the 256-level scale. A visual illustration of the images used for calculations is represented in Figure 4.14.

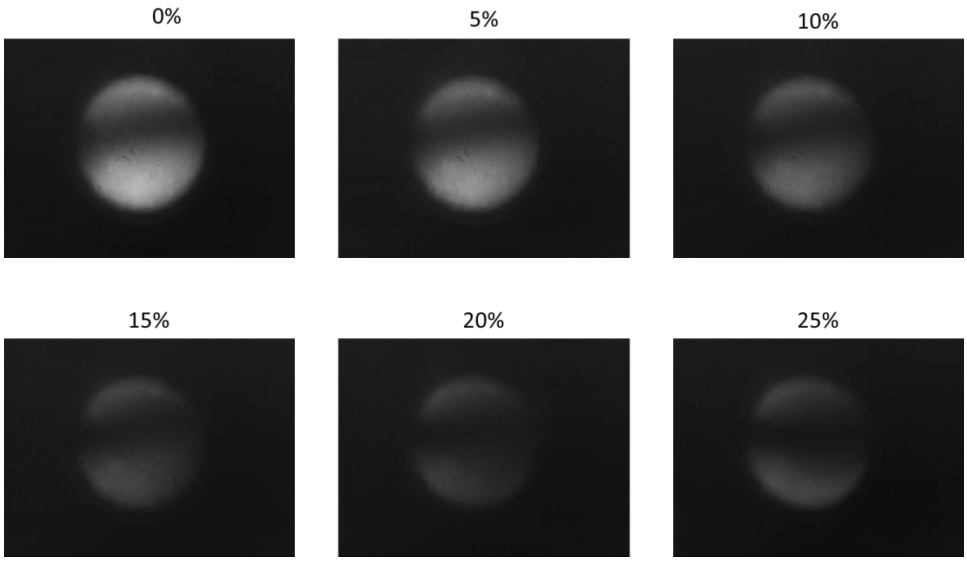

Figure 4.14: Visual image brightness dependence of the sucrose concentration.

As seen in Figure 4.14, the changes in the visual brightness of the images correlated very well with the quantitative characteristics shown in Figure 4.13, which allowed the conclusion that the camera has a potential for the microscopy imaging of inhomogeneous mixtures.

4.3.2 Grating Depth and Image Brightness

4.3.2.1 Grating Depth Distribution over Sample Surface

It is known that due to the Gaussian shape of the laser beam wavefront, used for the grating inscription on the azobenzene films, the grating depth across the grating surface decreases from the center of the grating to its edges. When the gratings are superimposed on top of each other, as in the case of the CSRG, the depth distribution becomes even more complicated. That is why it was necessary to understand how the image brightness correlates with the CSRG depth distribution over the grating surface and a series of tests was carried out to compare the brightness of images taken at different CSRG zones with the CSRG depth distribution map.

First, the CSRG surface map was scanned using the AFM as described in Section 3.2. The scanned areas were evenly distributed over the grating surface as illustrated in Figure 4.15. For each scanned area, an average depth value was measured separately for both orthogonal gratings.

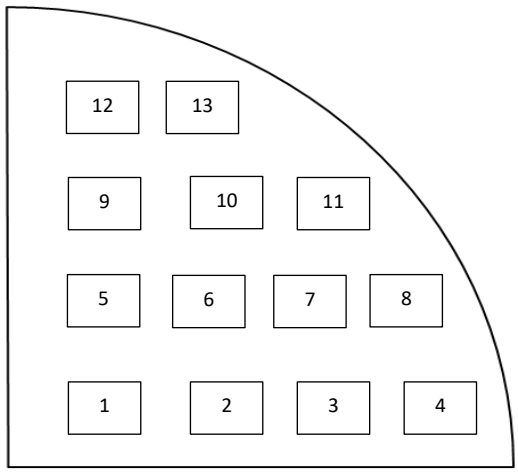

Figure 4.15: Not-to scale map of AFM scan areas chosen for CSRG depth distribution analysis

The obtained data were recorded in Origin® software and used for creating a two-dimensional contour depth map. Recall that the scanned area dimensions are 5x5µm^2 and the CSRG quarter-disk dimensions are ~7 x 7mm^2. In order to obtain a smoother map picture, the Origin® software extrapolation tools were used for the map plot. The resulting depth distribution map for the primary grating is shown in Figure 4.16(a). Recall that the convention accepted in this work designates the grating that was imprinted first during the fabrication as a primary grating. The grating imprinted atop of the primary grating is referred to as the secondary grating.

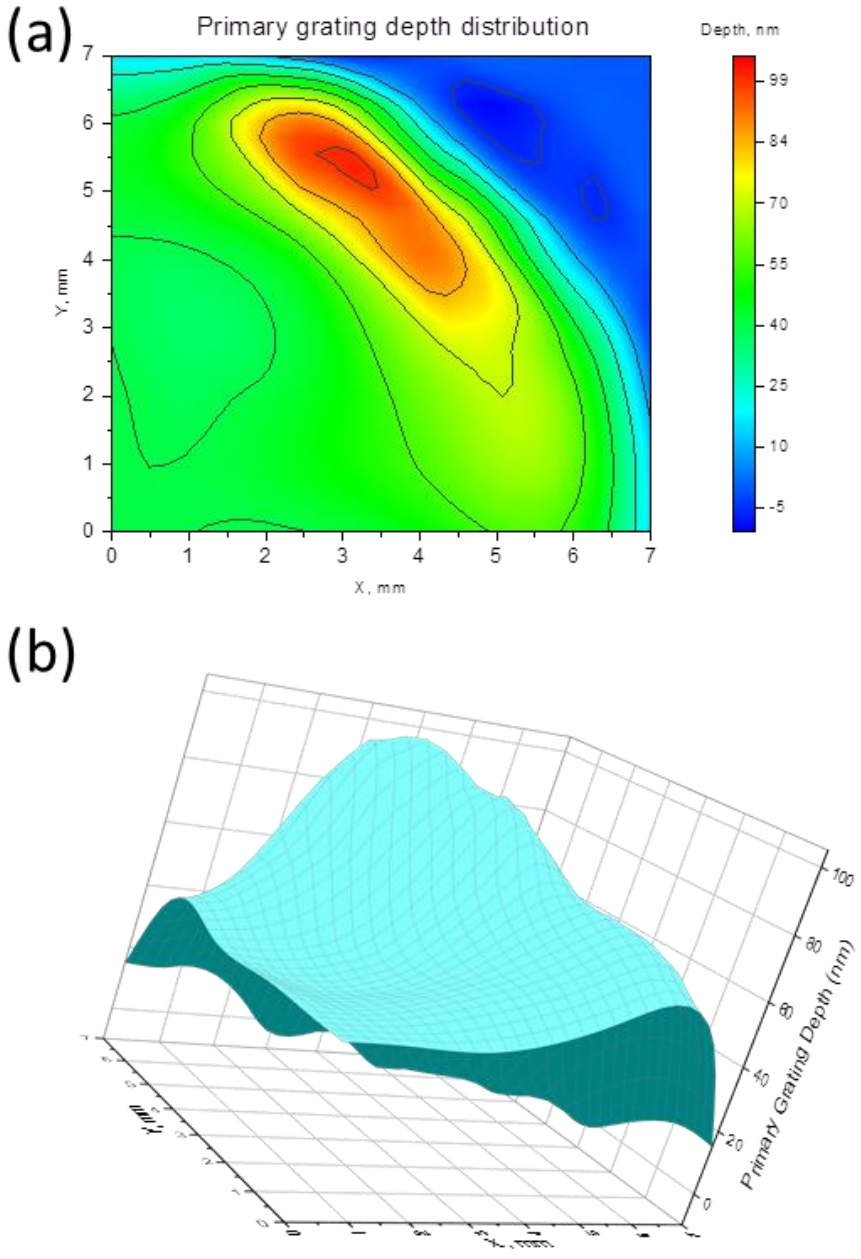

Figure 4.16: Primary grating depth distribution.

In this picture, the grating vector is oriented horizontally along the *x*-axis. The actual grating area is limited by the contour lines along the light-blue area and the blue color represents the surface beyond the CSRG. For a better visual representation of the depth distribution, a three-dimensional plot of the map is also included in Figure 4.16(b). As seen in the picture, the grating depth distribution is different from what could be expected for a single grating. In this particular case, one can see that there is an elongated area next to the edge of the grating area, which has deeper troughs than the areas closer to the center and to the axes. Evidently, this happened during the secondary grating inscription process, when the azobenzene molecules movement affected the peaks of the primary grating.

The same approach was used for obtaining the secondary grating depth distribution with the results represented in Figure 4.17.

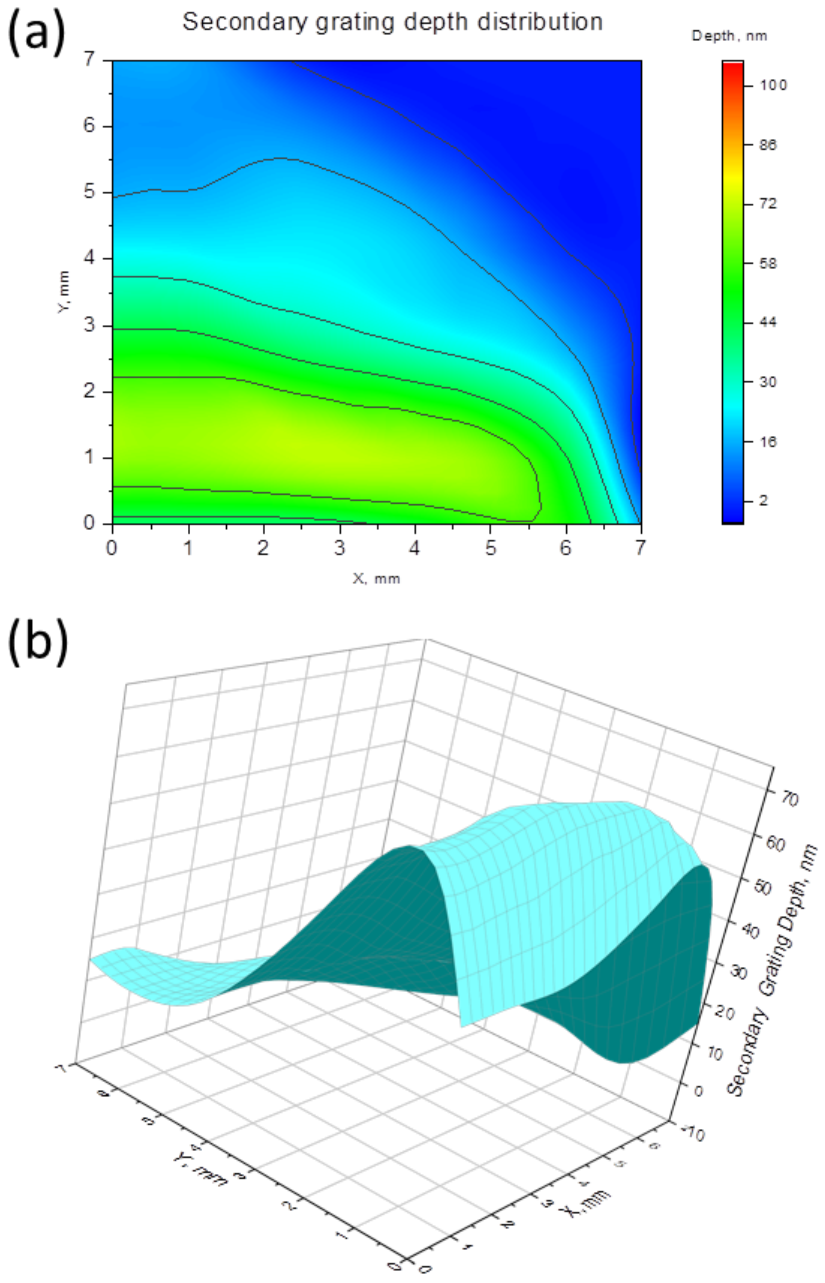

Figure 4.17: Secondary grating depth distribution.

This time the grating vector was oriented vertically along the *y*-axis. The color scales in both Figure 4.16 and Figure 4.17 are scaled to the same depth range in order to equalize the color palette of both maps for a better representation of the gratings' relative depth values.

4.3.2.2 Grating Depth and Image Brightness Correlation

Once the depth mapping of the sample was completed, the brightness distribution of the images generated by the light transmitted by the CSRG was measured across the grating. Ideally, the brightness distribution map would be more complete if the whole CSRG surface was covered by a single light beam spot, but the unfocused light intensity was not enough to excite an SPR of detectable strength. At the same time, the intensity of incoherent light varies significantly across the incoherent light beam, which also would hinder the brightness distribution analysis. That is why a series of images of evenly distributed areas of the CSRG was made to analyze the brightness variation across the CSRG surface. The chosen imaging zones are depicted in Figure 4.18. The yellow numbers atop of the images represent the image data matrices' average values. During the experiment, the first linear polarizer was oriented vertically and the second one – horizontally. The primary grating grooves were oriented vertically. That means, that the incident light generated the SPR on the secondary grating and the energy was outcoupled by the primary grating.

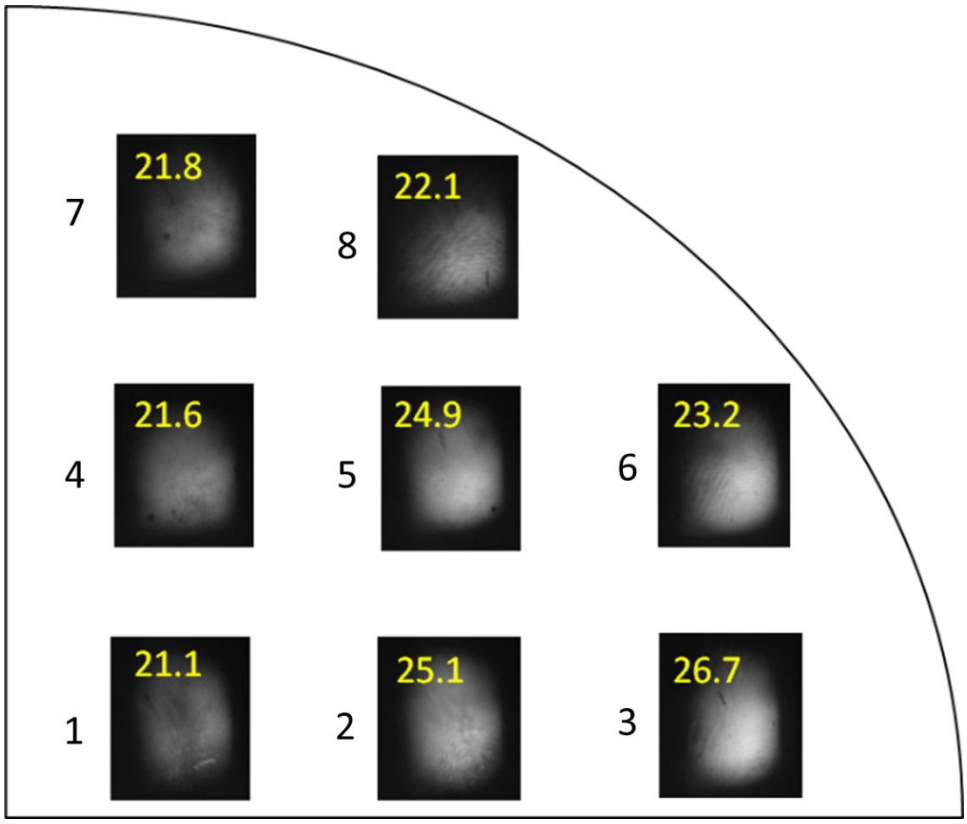

Figure 4.18: Brightness variation of the reemitted light across the CSRG surface

Recall, that one of the major grating parameters affecting the SPR strength is the grating depth, that should not be more than 100 nm otherwise it would create a band gap in the SPR spectrum, which decreases the device's sensitivity. On the other hand, shallow gratings excite weaker SPR, which also leads to a decrease in image brightness. This effect can be seen in Figure 4.18 for images # 4 and # 7, where the depth of the grating, which couples the incident light, is lower than 50 *nm*. At the same time, looking at image # 8, where the secondary grating depth is relatively small (approximately 30-40 *nm*), the outcoupled light brightness is slightly higher than for images # 4 and # 7. Obviously, it happened due to the larger depth values of the primary grating, where the light was outcoupled.

As seen in Figure 4.18, images # 2, 3, and 5 have the highest image data matrix average values. If compared to the grating depth distribution maps in

Figure 4.16 and Figure 4.17, it can be concluded that the best energy transfer happened in the zones where the depth values of both gratings are close to each other and lie in between 65-75 *nm*.

4.3.3 Scratches and Light-Blocking Object Imaging

To demonstrate the SPR wave propagation at the metal-dielectric boundary on the CSRG, a sample with scratches and light-blocking objects was prepared as described in Paragraph 3.6.2. When placed on the setup for the microscopy imaging using incoherent light, the resulting image is seen in Figure 4.19. Recall that the scratch's width on this sample was approximately 68 µm and the

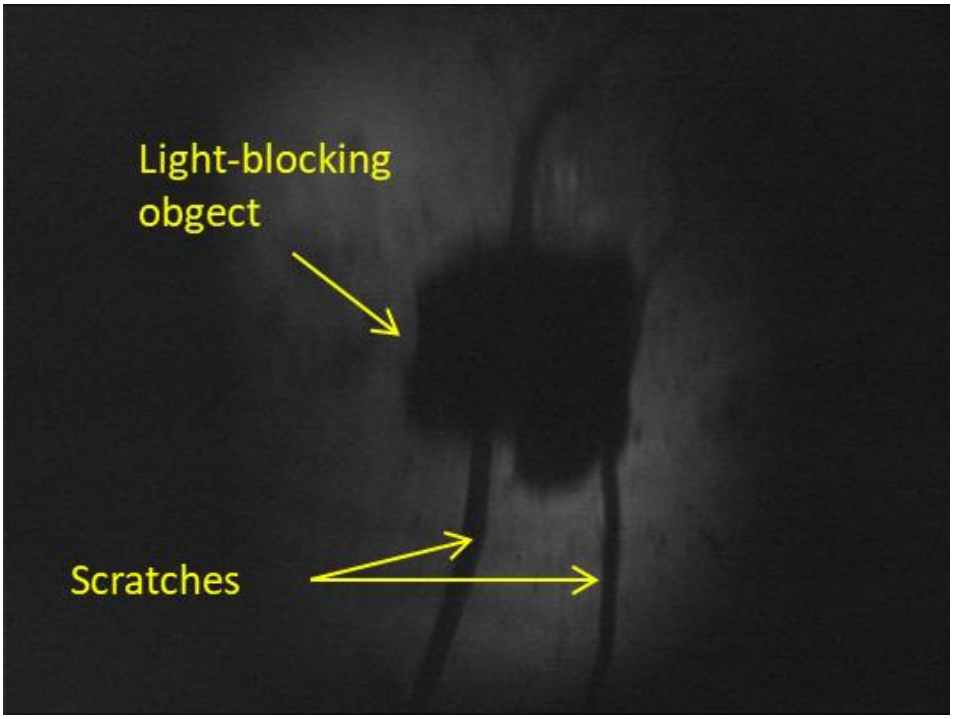

Figure 4.19: Scratches and a light-blocking object on the CSRG surface under incoherent light filtered at a wavelength of 632.8 nm.

light-blocking object dimensions were ~1.5 x 1.5 mm^2. In theory, the SPR propagation length is typically between 10 and 100 µm for visible light, depending upon the metal/dielectric [56]. This means that the SPR wave excited next to an edge of a light-blocking object placed directly on the grating should propagate a certain distance under this object. Evidently, the SPR wave should

not propagate across an edge of a scratch on the grating's surface, since the metal-dielectric interface is discontinued at this place. This can be demonstrated when the image of the light-blocking object edge is compared to the image of a scratch on the grating's surface as depicted in the zoomed area presented in Figure 4.20.

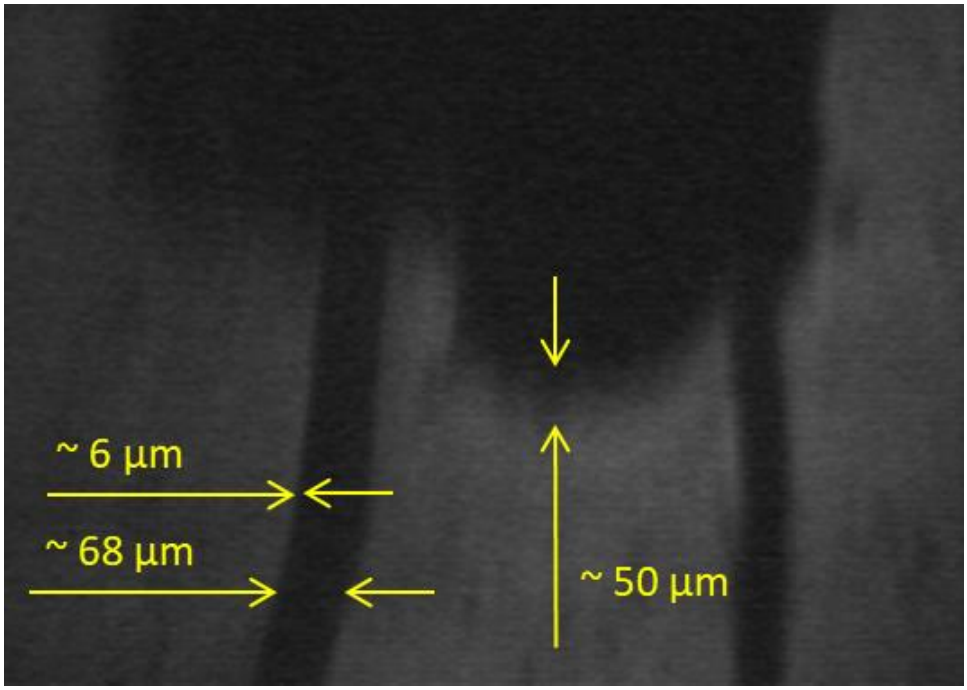

Figure 4.20: Scratches and the SPR wave propagation length mutual sizes.

All sizes shown in Figure 4.20 are calculated based on the known scratch width compared to the camera pixel size. For a visual demonstration of the resolution obtained with this particular image, Figure 4.21 shows a scratch area zoomed to a level where separate camera sensor pixels can be seen. Taking into account the pixel size of 10 µm, the linear scratch width of ~68 µm, and the scratch width in pixels ~20, it can be calculated that a single pixel in this picture represents an area of the CSRG of ~3x3 μm^2. This also means that the mutual location of the setup optical elements, the sample, and the camera in this particular case provided an approximately threefold magnification.

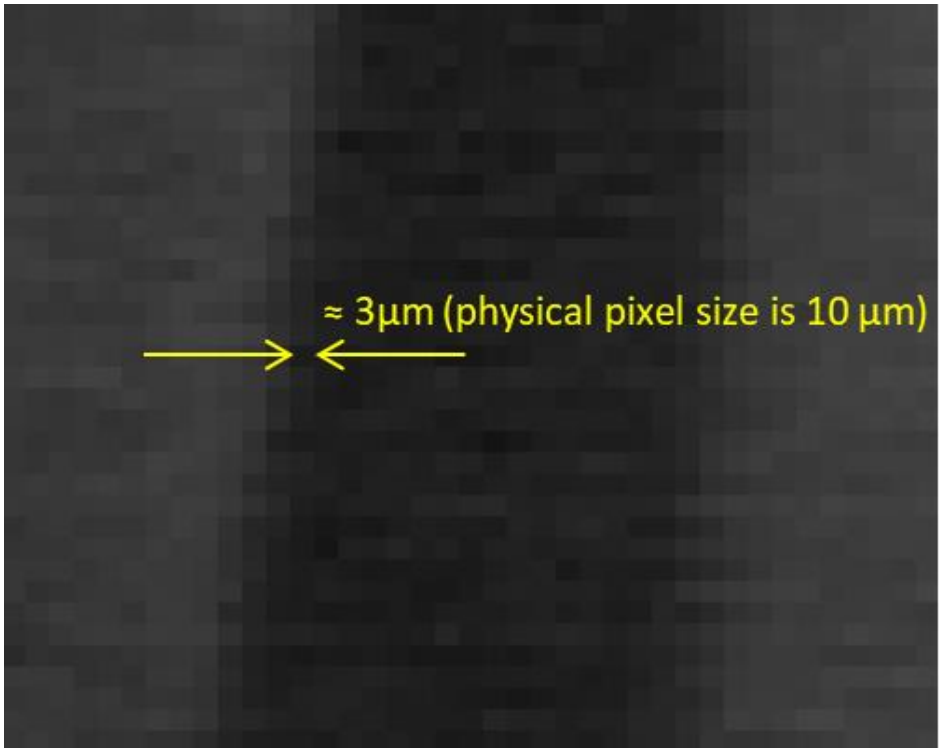

Figure 4.21: Zoomed scratch area.

As seen in Figure 4.20, there is a clearly distinguishable area of the brightness gradual attenuation around the light-blocking object. The area width reaches 50 µm, which complies with the theoretical SPR propagation length. At the same time, the blurred outlines of the scratch edges have a width of approximately 6 µm. This blur is caused by the resolution limiting factors such as the camera pixel size, camera internal flicker, and the whole setup focusing accuracy. This constitutes the first-ever imaging of the SPR propagation along a metal-dielectric interface.

4.3.4 Lamp filament

During the course of the microscopy imaging experiments, it was found that at certain positions of the lenses, the sample, and the camera along the light beam path, it was possible to capture the image of the filament of the halogen lamp that was used as a light source. Figure 4.22(a) illustrates the image registered with the incoherent light imaging setup as depicted earlier in Figure 3.11, with

one exception, that the sample was removed from the beam path. Obviously, the second polarizer blocked all the light passing through the first one and the resulting image was simply a black rectangle. When the CSRG device was placed back in its mount between the two polarizers, the halogen lamp filament appeared on the display as shown in Figure 4.22(b). This image serves as an excellent visual substantiation of the light polarization conversion theory [62], which was explained earlier in Paragraph 2.3. It represents a 2-dimensional demonstration of the perfect transfer of the SPR energy when light encounters a CSRG. This experiment allowed the observation that the energy distribution in the incoming light beam can be seen in the light outcoupled by the CSRG with very high resolution. The remaining major limiting factors, in this case, were the camera pixel size and the focusing elements arrangement along the light path. This ultimately illustrates that the SPR polarization conversion of incident light is selectively occurring on the CSRG surface based on the illuminated area formed by the lamp filament.

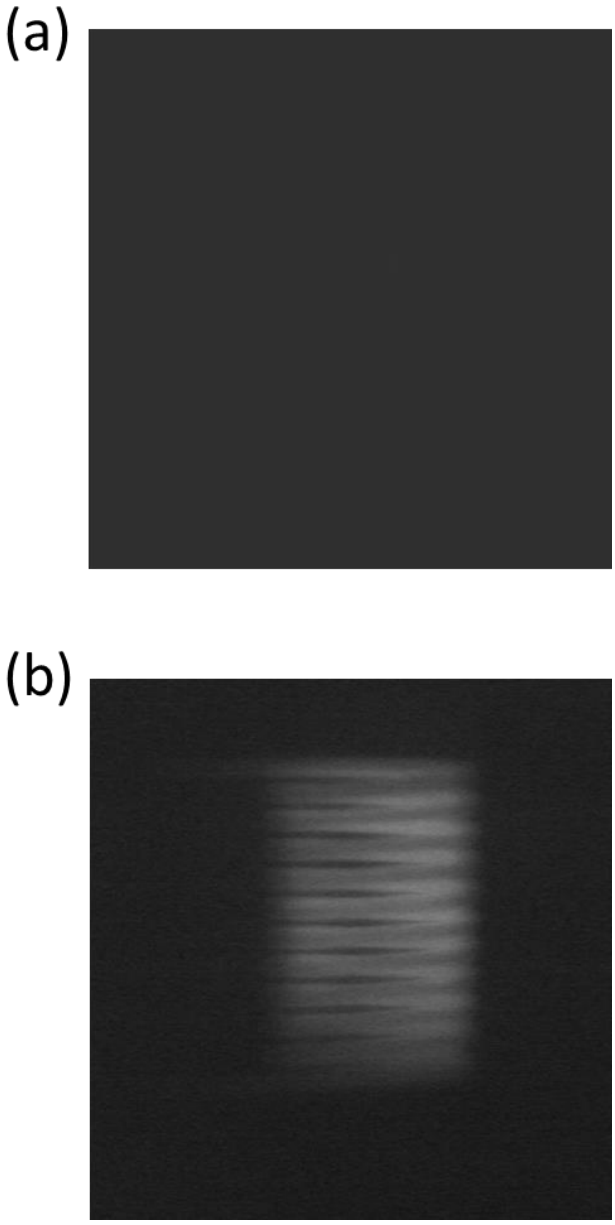

Figure 4.22: (a) – image taken with no sample between two linear orthogonal polarizers; (b) - monochromatic 632.8 nm image of the filament of the halogen lamp (12 V, 50 W, Oriel Corp.) transmitted by the CSRG when placed between two polarizers

4.3.5 Inhomogeneous Mixture Microscopy Imaging

In this part of the work, the recording and analysis of the images transmitted by the CSRG were made when the samples with mixtures were irradiated by an incoherent light beam at a wavelength of 632.8 nm using the setup and procedure described in Paragraph 3.6.2. Two types of mixtures were used for testing: a silicone oil water-based mixture and a mineral oil water-based mixture. It should be noted that from the very first attempt of imaging with incoherent light, it was obvious that the obtained images allowed much more detail observation of the irradiated area in comparison to the coherent light imaging outcomes. Undoubtedly, this improvement was primarily related to the absence of the light interference patterns and the image granularity described earlier in Paragraph 4.2.3.

First, the silicone oil mixture was tested for imaging. The obtained video images allowed the observation of the silicone oil particles floating up in water during the mixture separation. Figure 4.23 represents a sequence of images extracted from the video. In the zoomed area the movement of a selected oil particle indicated with the yellow pointer can be observed. This specific particle represents a shadowing object, which is easily distinguishable in motion from the other dark patterns in the picture. The static patterns are created by other particles held on the grating surface and on the cover glass.

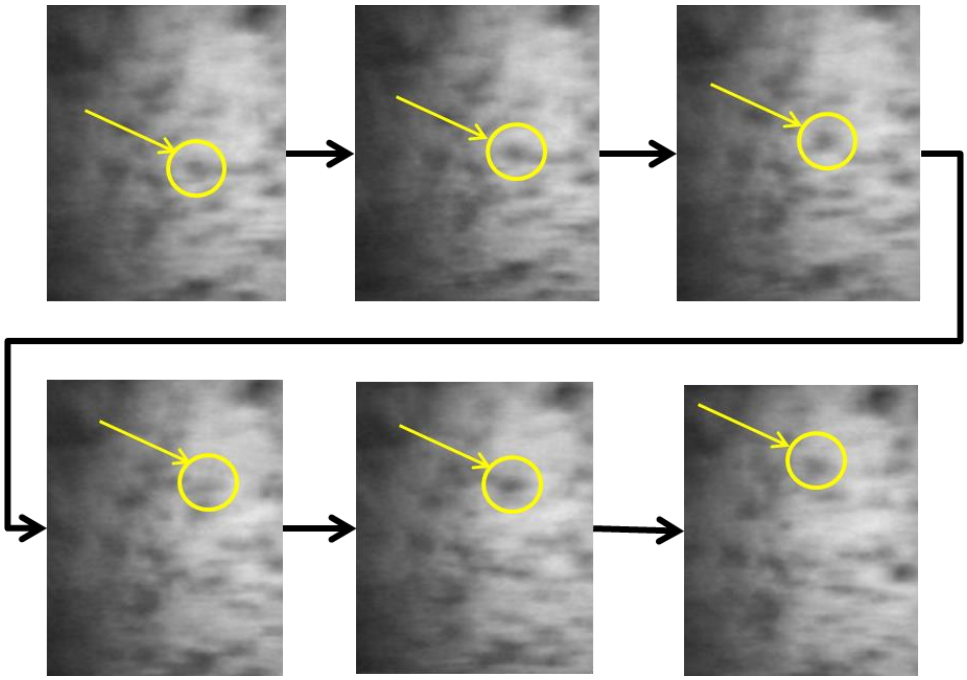

Figure 4.23: Silicone oil particles movement illustrated with one selected particle changing position with an interval of approximately 1 sec

Before the mixture was placed in the PDMS reservoir, an image had been made with pure water on the grating. Afterward, this image was used as a baseline for obtaining the difference images of the silicone oil particles in the mixture. The result of the simple mathematical subtraction of two images made with the help of Origin® software is shown in Figure 4.24. The mixture image was made 30 min after the sample had been placed on the fixture. At that moment no more moving oil particles were seen in the picture displayed on the monitor. This meant that the oil separation from the water had been completed by that time and only particles held on the CSRG and the cover glass surfaces could be recorded. In Figure 4.24, the dark zones in the resulting difference image demonstrate the silicone oil particles on both surfaces. The shadows caused by the oil on the cover glass surface are overlapped with the SPR image of the RI spatial distribution along the metal-mixture interface. Hence, the problem of distinguishing between the shadowing particles and the SPR images remains unresolved and represents a subject of future work.

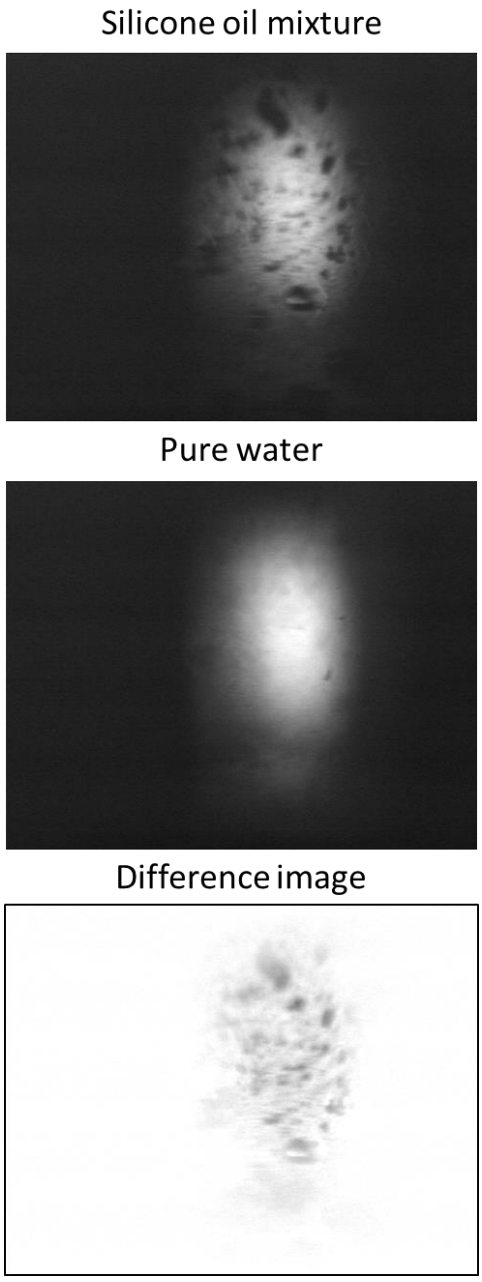

Figure 4.24: Difference image resulting from a subtraction of a pure water image from an image of a silicone oil mixture.

Analogous series of microscopy imaging tests were carried out utilizing a light mineral oil aqueous mixture. In general, static and video images obtained with this mixture demonstrated more distinguishable oil particles, both on the reservoir surfaces and in the water if compared to the images of the silicone oil mixtures. This happened due to the higher surface tension of the mineral oil [73] with respect to the silicone oil surface tension [74] and, therefore, its lesser ability to spread over the surfaces of the grating and the cover glass. Figure 4.25 illustrates a mineral oil particle motion during the mixture separation phase. The picture was generated by the same method as was done before for the silicon oil particle motion demonstration.

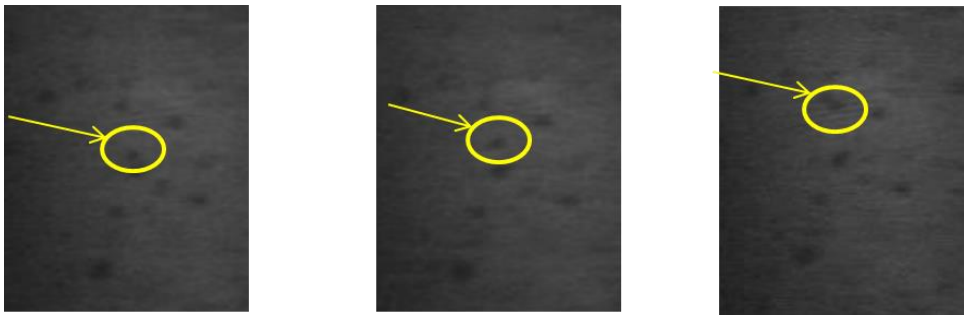

Figure 4.25: Mineral oil particle movement illustrated with one selected particle changing position with an interval of approximately 1 sec.

Figure 4.26 illustrates the difference image of the mineral oil mixture. Although this mixture gave better difference image results, the problem of distinguishing the SPR image from the patterns generated by shadowing objects persists.

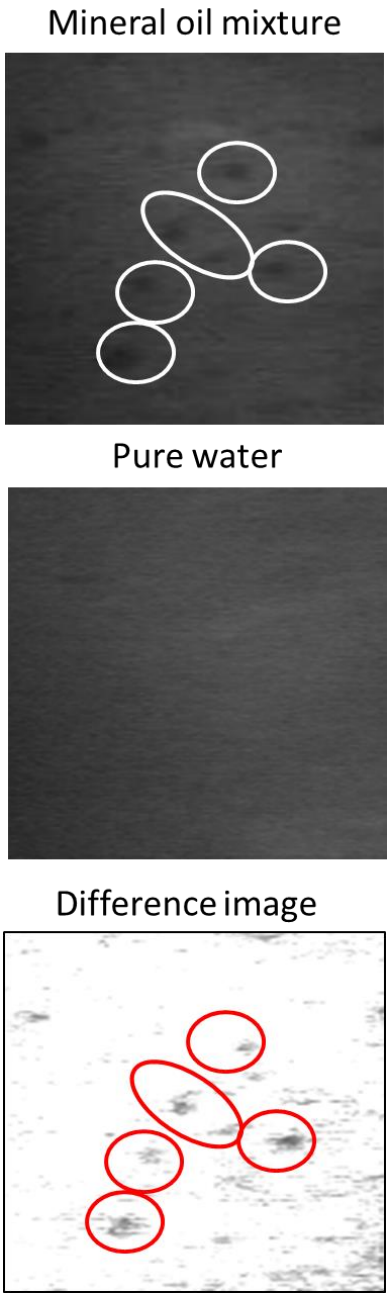

Figure 4.26: Difference image resulted from a subtraction of a pure water image from an image of a light mineral oil mixture.

5 Conclusion

5.1 Summary

The goal of this thesis was to demonstrate the potential application of crossed surface relief gratings inscribed on azobenzene thin films for the purpose of SPR microscopy. This work was focused on using a plasmonic CSRG as the main element of a system for obtaining high-contrast two-dimensional microscopic images of aqueous inhomogeneous mixtures. The experiments were carried out using coherent and incoherent light sources for the sample illumination. The results were analyzed and compared in order to validate the prospective development of this method.

The physical phenomenon lying at the basis of SPR microscopy imaging is known as a Surface Plasmon Resonance wave, which may be excited on a metal-dielectric interface under certain conditions. The light polarization conversion effect created by two superimposed orthogonal linear gratings placed between crossed polarizers was used to increase the polarization contrast and the sensitivity of the device. The technique used for the grating fabrication utilizes a laser interference pattern, which was directly imprinted on azobenzene molecular glass films subsequently covered by a 60 nm silver coating. Both orthogonal gratings' parameters were optimized in a way that the obtained CSRG could transmit only a narrow band of light at a wavelength of 632.8 nm when an aqueous mixture was used as a test sample in contact with the grating. The best results were obtained when the CSRGs were fabricated with 450 nm pitch, which resulted in the SPR signal peak with the wavelength of 632.8 nm corresponding to its highest slope.

Different types of inhomogeneous aqueous mixtures including components such as silicone oil, mineral oil, corn starch, and silica gel powders were used as test samples for the microscopic imaging. All of them provided similar imaging results, allowing the observation of SPR intensity variations in

the resultant monochromatic images. The main practical difference between the mixtures was that the contamination caused by the oil mixtures did not allow the reuse of the CSRGs, while the use of starch and gel mixtures allowed the same CSRG to be used multiple times.

The CSRG device with a test sample mixture resting on the surface of the grating was illuminated with linearly polarized light at a wavelength of 632.8 nm. This ensured a narrower bandwidth of the transmitted signal resulting in increased image contrast. The transmitted light from the CSRG device was filtered by an orthogonal linear polarizer to eliminate any incident light from the signal. The filtered beam was, therefore, carrying only information about the spatial distribution of the SPR intensities on the CSRG and was recorded using a high-dynamic-range camera. The attempts of imaging using a coherent light source ended with unsatisfactory results in terms of the image quality. The resolution of the obtained images was thought to be adversely affected by the light interference patterns caused by the coherent light in the experimental setup.

At this stage of the research, it was determined that the experiments with the incoherent light filtered by a narrowband interference filter at a wavelength of 632.8 nm provided more valuable results. This setup allowed the study of how the relative depth of both orthogonal gratings affects the resulting image's brightness. It was concluded that the highest quality images can be obtained when orthogonal gratings of a CSRG have identical depths of approximately 70 nm each. The SPR microscopy images of the inhomogeneous mixtures obtained in the course of the experiments with incoherent light allowed the observation of the SPR intensity variation caused by objects of two different types. A part of the SPR intensity variation was generated by the mixtures' RI spatial distribution along the grating-mixture interface. Another part of the intensity variation was caused by the light shadowing created by the particles remote from the grating-mixture boundary. At the present phase of the research, the images of these two different types are overlapped and cannot be distinguished from each other. The separation of these two types of images may be the subject of future work.

Also, a demonstration of the SPR wave propagation length was made using light-blocking objects and scratches on the grating surface. This is believed to be the first-ever direct imaging of the SPR propagation along a metal-dielectric interface. The estimated SPR propagation length along the boundary of approximately 40-50 microns was close to the theoretical values [56].

Another remarkable result obtained with the incoherent light was the halogen lamp filament image. This provided an excellent two-dimensional visual demonstration of the light polarization conversion phenomena when linearly polarized light from an object was reemitted by a CSRG in a beam carrying the object's image with the polarization perpendicular to the polarization direction of the incident beam. The almost perfectly resolved energy transfer from vertically to horizontally polarized light could be observed pixel by pixel on the obtained image.

5.2 Future Work

Future work could be focused on a solution for the persisting problem of distinguishing between the patterns caused by the changing RI of the dielectric at the metal-dielectric interface and the patterns from the shadowing objects. This could be addressed by changing the sample preparation technique and the sample fixture modification so that the sample could be placed horizontally to the ground. Such a position could allow replacing the contaminated cover glass with a clean one. This will require a redirection of the light beam so that it would be vertically incident on the CSRG. Obviously, this would involve incorporation of additional optical elements and fixtures in the setup.

Separate efforts should be made for the calculation and design of the lens system. The SPR microscopy should theoretically allow the observation of objects with subwavelength dimensions, but without the appropriate optical magnification, this advantage remains unrealized. A properly designed optical system would enlarge the image transferred by a CSRG to the maximum number of pixels on the camera sensor, thus increasing the resolution and making use of the full potential of the SPR imaging technique.

Finally, more extensive research is required for a better understanding of the influence of the depths ratio of two orthogonal gratings on the resulting image brightness across the CSRG. This information will help to fabricate CSRG of higher energy transfer efficiency and obtain higher contrast SPR microscopy images.

References

1. R. W. Wood, "XLII. On a remarkable case of uneven distribution of light in a diffraction grating spectrum," The London, Edinburgh, and Dublin Philosophical Magazine and Journal of Science **4,** 396-402 (1902).

2. U. Fano, "The theory of anomalous diffraction gratings and of quasi-stationary waves on metallic surfaces (Sommerfeld's waves)," JOSA **31,** 213-222 (1941).

3. A. Sommerfeld, *Vorlesungen über Theoretische Physik, Band VI: Partielle Differentialgleichungen der Physik* (Dieterich'sche Verlagsbuchhandlung, 1947).

4. A. Sommerfeld, "Über die Ausbreitung der Wellen in der drahtlosen Telegraphie," Annalen der Physik **333,** 665-736 (1909).

5. D. Bohm and D. Pines, "A collective description of electron interactions: III. Coulomb interactions in a degenerate electron gas," Physical Review **92,** 609 (1953).

6. R. H. Ritchie, "Plasma losses by fast electrons in thin films," Physical review **106,** 874 (1957).

7. E. A. Stern and R. A. Ferrell, "Surface plasma oscillations of a degenerate electron gas," Physical Review **120,** 130 (1960).

8. R. A. Ferrell, "Predicted radiation of plasma oscillations in metal films," Physical Review **111,** 1214 (1958).

9. A. Otto, "Excitation of nonradiative surface plasma waves in silver by the method of frustrated total reflection," Zeitschrift für Physik A Hadrons and nuclei **216,** 398-410 (1968).

10. E. Kretschmann and H. Raether, "Radiative decay of non radiative surface plasmons excited by light," Zeitschrift für Naturforschung A **23,** 2135-2136 (1968).

11. Y. Ma, "Surface Plasmon Polaritons Based Nanophotonic Devices and their Applications," (2015).

12. T. W. Ebbesen, H. J. Lezec, H. F. Ghaemi, T. Thio, and P. A. Wolff, "Extraordinary optical transmission through sub-wavelength hole arrays," Nature **391,** 667 (1998).

13. J. Braun, B. Gompf, G. Kobiela, and M. Dressel, "How holes can obscure the view: suppressed transmission through an ultrathin metal film by a subwavelength hole array," Phys. Rev. Lett. **103,** 203901 (2009).

14. G. Ctistis, E. Papaioannou, P. Patoka, J. Gutek, P. Fumagalli, and M. Giersig, "Optical and magnetic properties of hexagonal arrays of subwavelength holes in optically thin cobalt films," Nano letters **9,** 1-6 (2008).

15. S. Vedantam, H. Lee, J. Tang, J. Conway, M. Staffaroni, and E. Yablonovitch, "A plasmonic dimple lens for nanoscale focusing of light," Nano letters **9,** 3447-3452 (2009).

16. M. Rycenga, C. M. Cobley, J. Zeng, W. Li, C. H. Moran, Q. Zhang, D. Qin, and Y. Xia, "Controlling the synthesis and assembly of silver nanostructures for plasmonic applications," Chem. Rev. **111,** 3669-3712 (2011).

17. V. V. Klimov, *Nanoplasmonics* (Physmatlit, 2013).

18. P. Martyniuk, J. Antoszewski, M. Martyniuk, L. Faraone, and A. Rogalski, "New concepts in infrared photodetector designs," Applied Physics Reviews **1,** 041102 (2014).

19. L. Novotny and B. Hecht, *Principles of nano-optics* (Cambridge university press, 2012).

20. L. Fedorenko, B. Snopok, M. Yusupov, O. Lytvyn, and Y. Burlachenko, "Laser Assisted Au Nanocrystal Formation in Conditions of Surface Plasmon Resonance," Acta Physica Polonica-Series A General Physics **115,** 1075 (2009).

21. H. Raether, "Surface plasmons on smooth surfaces," in *Surface plasmons on smooth and rough surfaces and on gratings,* Anonymous (Springer, 1988), pp. 4-39.

22. T. Nikolajsen, K. Leosson, I. Salakhutdinov, and S. I. Bozhevolnyi, "Polymer-based surface-plasmon-polariton stripe waveguides at telecommunication wavelengths," Appl. Phys. Lett. **82,** 668-670 (2003).

23. D. Beaglehole, "Coherent and incoherent radiation from optically excited surface plasmons on a metal grating," Phys. Rev. Lett. **22,** 708 (1969).

24. M. Born and E. Wolf, *Principles of optics: electromagnetic theory of propagation, interference and diffraction of light* (Elsevier, 2013).

25. G. Xiao and W. J. Bock, *Photonic Sensing: Principles and Applications for Safety and Security Monitoring* (John Wiley & Sons, 2012).

26. T. Tabbakh and P. LiKamWa, "Liquid sensor based on optical surface plasmon resonance in a dielectric waveguide," in *Micro-and Nanotechnology Sensors, Systems, and Applications X,* Anonymous (International Society for Optics and Photonics, 2018), pp. 106392P.

27. C. R. Lavers, K. Itoh, S. C. Wu, M. Murabayashi, I. Mauchline, G. Stewart, and T. Stout, "Planar optical waveguides for sensing applications," Sensors Actuators B: Chem. **69,** 85-95 (2000).

28. A. W. Peterson, M. Halter, A. Tona, and A. L. Plant, "High resolution surface plasmon resonance imaging for single cells," BMC cell biology **15,** 35 (2014).

29. A. Lipson, S. G. Lipson, and H. Lipson, *Optical physics* (Cambridge University Press, 2010).

30. L. Rayleigh, "XXXI. Investigations in optics, with special reference to the spectroscope," The London, Edinburgh, and Dublin Philosophical Magazine and Journal of Science **8,** 261-274 (1879).

31. W. M. Saslow, *Electricity, Magnetism, and Light* (Elsevier, 2002).

32. B. Rothenhäusler and W. Knoll, "Surface–plasmon microscopy," Nature **332,** 615 (1988).

33. S. I. Valanskiy, "Surface Plasmon Microscope", Soros Educational Journal, 76-82 (1999).

34. G. Roberts, *Langmuir-blodgett films* (Springer Science & Business Media, 2013).

35. E. Wijaya, C. Lenaerts, S. Maricot, J. Hastanin, S. Habraken, J. Vilcot, R. Boukherroub, and S. Szunerits, "Surface plasmon resonance-based biosensors: From the development of different SPR structures to novel surface functionalization strategies," Current Opinion in Solid State and Materials Science **15,** 208-224 (2011).

36. A. J. Tudos and R. B. Schasfoort, "Introduction to surface plasmon resonance," Handbook of surface Plasmon resonance1-14 (2008).

37. A. Duval, F. Bardin, A. Aide, A. Bellemain, J. Moreau, and M. Canva, "Anisotropic surface-plasmon resonance imaging biosensor," SPIE Newsroom (2007).

38. J. M. Brockman and S. M. Fernández, "Grating-coupled surface plasmon resonance for rapid, label-free, array-based sensing," Am. Lab. **33,** 37-40 (2001).

39. G. Medhi, J. W. Cleary, R. E. Peale, G. Boreman, W. R. Buchwald, S. Wentzell, O. Edwards, and I. Oladeji, "Infrared surface plasmon resonance hosts for sensors," in *Photonics 2010: Tenth International Conference on Fiber Optics and Photonics,* Anonymous (International Society for Optics and Photonics, 2011), pp. 81731N.

40. P. Rochon, E. Batalla, and A. Natansohn, "Optically induced surface gratings on azoaromatic polymer films," Appl. Phys. Lett. **66,** 136-138 (1995).

41. J. P. Monteiro, J. Ferreira, R. G. Sabat, P. Rochon, M. J. L. Santos, and E. M. Girotto, "SPR based biosensor using surface relief grating in transmission mode," Sensors Actuators B: Chem. **174,** 270-273 (2012).

42. S. Nair, J. Gomez-Cruz, Á Manjarrez-Hernandez, G. Ascanio, R. Sabat, and C. Escobedo, "Selective Uropathogenic E. coli Detection Using Crossed Surface-Relief Gratings," Sensors **18,** 3634 (2018).

43. M. Wood, "Optics-Diffraction grating.jpg," https://sharepoint.umich.edu/lsa/physics/demolab/Experiment%20Picture%20Library/Forms/DispForm.aspx?ID=26. [Accessed: 12-Feb-2019].

44. L. Frank, S. J. Pedrotti, L. M. Pedrotti, and L. S. Pedrotti, "Introduction to optics," (1993).

45. Y. Zou, R. Hutton, F. Currell, I. Martinson, and S. Hagmann, *Handbook for highly charged ion spectroscopic research* (Taylor & Francis, 2016).

46. E. Bailey and R. G. Sabat, "Surface plasmon bandwidth increase using chirped-pitch linear diffraction gratings," Optics express **25,** 6904-6913 (2017).

47. J. Leibold and R. G. Sabat, "Laser-induced controllable chirped-pitch circular surface-relief diffraction gratings on AZO glass," Photonics Research **3,** 158-163 (2015).

48. N. Swanson and R. G. Sabat, "Inscription and analysis of non-uniform diffraction gratings in azobenzene molecular glass thin films," Optics express **26,** 7876-7887 (2018).

49. K. G. Yager and C. J. Barrett, *Azobenzene polymers as photomechanical and multifunctional smart materials* (RSC Publishing: Cambridge, UK, 2008).

50. M. Kashif, A. A. A. Bakar, N. Arsad, and S. Shaari, "Development of phase detection schemes based on surface plasmon resonance using interferometry," Sensors **14,** 15914-15938 (2014).

51. A. Natansohn and P. Rochon, "Photoinduced motions in azo-containing polymers," Chem. Rev. **102,** 4139-4176 (2002).

52. C. J. Barrett, A. L. Natansohn, and P. L. Rochon, "Mechanism of optically inscribed high-efficiency diffraction gratings in azo polymer films," J. Phys. Chem. **100,** 8836-8842 (1996).

53. David J. Griffiths, *Introduction to Electrodynamics, 3rd Edition* (Pearson, 1999).

54. Anonymous "ILO Encyclopaedia of Occupational Health and Safety," http://www.ilocis.org/documents/chpt49e.htm. [Accessed: 24-Feb-2019].

55. J. Homola and M. Piliarik, "Surface plasmon resonance (SPR) sensors," in *Surface plasmon resonance based sensors,* Anonymous (Springer, 2006), pp. 45-67.

56. S. A. Maier, *Plasmonics: fundamentals and applications* (Springer Science & Business Media, 2007).

57. M. Kuno, "Introductory nanoscience: Physical and chemical concepts," MRS Bull **37,** 169-170 (2012).

58. N. W. Ashcroft and N. D. Mermin, "Solid state physics [by] Neil W. Ashcroft [and] N. David Mermin." (1976).

59. W. L. Barnes, A. Dereux, and T. W. Ebbesen, "Surface plasmon subwavelength optics," Nature **424,** 824 (2003).

60. H. Raether, "Surface plasmons on gratings," in *Surface plasmons on smooth and rough surfaces and on gratings,* Anonymous (Springer, 1988), pp. 91-116.

61. P. L. Rochon and L. Lévesque, "Standing wave surface plasmon mediated forward and backward scattering," Optics Express **14,** 13050-13055 (2006).

62. R. G. Sabat, N. Rochon, and P. Rochon, "Dependence of surface plasmon polarization conversion on the grating pitch," JOSA A **27,** 518-522 (2010).

63. R. Kirby, R. G. Sabat, J. Nunzi, and O. Lebel, "Disperse and disordered: a mexylaminotriazine-substituted azobenzene derivative with superior glass and surface relief grating formation," Journal of Materials Chemistry C **2,** 841-847 (2014).

64. Bruker, "ScanAsyst:Exclusive, Self-Optimizing AFM Imaging," 1-4.

65. A. Giannattasio, I. R. Hooper, and W. L. Barnes, "Transmission of light through thin silver films via surface plasmon-polaritons," Optics express **12,** 5881-5886 (2004).

66. Y. Bdour, C. Escobedo, and R. G. Sabat, "Wavelength-selective plasmonic sensor based
on chirped-pitch crossed surface relief
gratings," OPTICS EXPRESS **27,** (2019).

67. S. C. Kitson, W. L. Barnes, G. W. Bradberry, and J. R. Sambles, "Surface profile dependence of surface plasmon band gaps on metallic gratings," J. Appl. Phys. **79,** 7383-7385 (1996).

68. M. Daimon and A. Masumura, "Measurement of the refractive index of distilled water from the near-infrared region to the ultraviolet region," Appl. Opt. **46,** 3811-3820 (2007).

69. W. S. Werner, K. Glantschnig, and C. Ambrosch-Draxl, "Optical constants and inelastic electron-scattering data for 17 elemental metals," Journal of Physical and Chemical Reference Data **38,** 1013-1092 (2009).

70. L. F. Hoyt, "New table of the refractive index of pure glycerol at 20 C," Industrial & Engineering Chemistry **26,** 329-332 (1934).

71. S. Nair, C. Escobedo, and R. G. Sabat, "Crossed surface relief gratings as nanoplasmonic biosensors," ACS sensors **2,** 379-385 (2017).

72. J. Jane, L. Shen, L. Wang, and C. C. Maningat, "Preparation and properties of small-particle corn starch," Cereal Chem. **69,** 280-283 (1992).

73. C. G. d. Mendonça, C. G. Raetano, and C. G. d. Mendonça, "Surface tension of mineral oils and vegetable oils," Engenharia Agrícola **27,** 16-23 (2007).

74. E. Ricci, R. Sangiorgi, and A. Passerone, "Density and surface tension of dioctylphthalate, silicone oil and their solutions," Surface and Coatings Technology **28,** 215-223 (1986).